Development of robust Cu_2O – and ZnO – coated polypropylene fabrics by AP-SALD for antimicrobial applications

by

Guvanch Gurbandurdyyev

A thesis

presented to the University of Waterloo

in fulfilment of the

thesis requirement for the degree of

Master of Applied Science

in

Mechanical and Mechatronics Engineering

Waterloo, Ontario, Canada, 2021

AUTHOR'S DECLARATION

I hereby declare that I am the sole author of this thesis. This is a true copy of the thesis, including any required final revisions, as accepted by my examiners.

I understand that my thesis may be made electronically available to the public.

Abstract

Nowadays, the textile industry is revolutionizing by adding special functionalities and properties to textiles. Especially with the emergence of COVID-19, textile functionalization has attracted the focus of researchers for antimicrobial applications. Cuprous oxide (Cu_2O) and zinc oxide (ZnO) are two oxides, which are known to have antiviral and antibacterial properties, respectively.

Atmospheric-pressure spatial atomic layer deposition (AP-SALD) is a relatively new method, which allows high-quality, high-throughput, conformal, pinhole-free, uniform coatings at the nanometer-scale and eliminates the slow speed and vacuum requirements that hinder conventional atomic layer deposition. In this thesis, spun-bond polypropylene (PP) fabrics that are used as an outer layer of N95 respirators were coated with Cu_2O and ZnO nanocoatings by AP-SALD. To the best of my knowledge, this is the first time that fabrics have been coated by AP-SALD, which is a promising method for mass production. An important property that textile coatings must have is good adhesion, which was fulfilled by AP-SALD in this work. Unlike coatings on rigid substrates, measuring the thickness of coatings on textiles is challenging due to the porosity and uneven surface of fabrics. In-situ reflectometry was utilized to study the growth rate of coatings by applying the Virtual Interface Method (VIM), which uses the reflectance intensity at a single wavelength over time. The growth rate per cycle (GPC) of depositions was estimated by analyzing the resulting damped oscillatory pattern.

The purpose of coating the spun-bond PP is to use it, especially Cu_2O-coated PP, for antimicrobial N95 respirators. For this reason, it is important to ensure that coatings do not affect the filtration efficiency of fabrics. Penetration percentages (100 – filtration efficiency) of coated fabrics were measured. Results indicate that the coatings do not have an obvious impact on the filtration efficiency. Finally, since it is well-known that Cu_2O shows an excellent antiviral performance against

many viruses, including SARS-CoV-2, the cytotoxicity of Cu_2O coatings deposited by AP-SALD against living cells was examined with Alamar blue (AB) and 5-carboxyfluorescein diacetate (CFDA) assays to check their compatibility for human use. Based on the results, Cu_2O – coated PP fabrics coated at 100 °C seem to be safe for use in N95 respirators.

Acknowledgments

First of all, I am extremely grateful to my supervisor Dr Kevin Musselman for his insightful advice, patience that cannot be underestimated, as well as continuous support literally in every aspect. I would not be writing this thesis without his guidance and encouragements. Thank you for providing me an excellent environment for doing research.

I also wish to thank the research group members, especially Alex Jones, Louis Delumeau, and Hatameh Asgarimoghaddam for their help with SALD, Fan Ye for sparing his time for SEM measurements, Jhi Yong Loke and Chee Hau Teoh for their valuable advice on technical matters.

I would like to extend my sincere thanks to Dr. Stephanie DeWitte-Orr and Samantha Lum for their collaboration and performing cell viability tests on my samples. Thank you to Dr. David Muňoz-Rojas and, Abderrahime Sekkat for preparing some CuO_x samples for me, and Eclipse Automation Inc for providing fabrics for this work. I would also like to acknowledge the help of James Cheon for training and helping me to perform filter tests.

Lastly, but most importantly, I am deeply indebted to my family for their endless support. To my mother, Ogulsapar Gurbandurdyyeva, you are not here with us, but I still feel your love and support. Thank you, you deserve the most appreciation! To my father, Nurgeldi Gurbandurdyyev, thank you for encouraging and supporting me to succeed regardless the challenges you faced. To my big brothers, Agajan and Bayram, my life would be boring and difficult without you. Thank you for being supportive brothers. Finally, to Bibi Ovezova, we made this together. Thank you for motivating and believing in me.

Dedication

I dedicate this work to my mother, who neglected her health for me to succeed. I made it because you believed in me.

Table of Contents

List of Figures

List of Tables

List of Abbreviations

AB	Alamar Blue
AP-SALD	Atmospheric Pressure Spatial Atomic Layer Deposition
BCC	Body-Centered Cubic
BSE	Back-Scattered Electron
CFDA-AM	5-Carboxyfluorescein Diacetate, Acetoxymethyl Ester
$Cu(hfac)_2$	Copper(II) Hexafluoroacetylacetonate Hydrate
CVD	Chemical Vapor Deposition
DC	Direct Current
DEZ	Diethyl Zinc
dsDNA	double-stranded DNA
EBE	Electron Beam Evaporation
EDX	Energy Dispersive X-Ray
Eg	Bandgap
eV	Electronvolt
FCC	Face-Centered Cubic
(GI)XRD	(Grazing Incidence) X-ray Diffraction
GPC	Growth Per Cycle
HCP	Hexagonal Close Packed
HIV	Human Immunodeficiency Virus
H1N1	Subtype of Influenza A Virus
MB	Melt-Blown
MBE	Molecular-Beam Epitaxy
MERS-CoV	Middle East Respiratory Syndrome–Related Coronavirus
MFC	Mass Flow Controller
MTT bromide	3-(4,5-dimethylthiazol-2-yl)-2,5-diphenyl-2H- tetrazolium

NIOSH	National Institute for Occupational Safety and Health
PLD	Pulsed Laser Deposition
PP	Polypropylene
PPE	Personal Protective Equipment
PVD	Physical Vapor Deposition
QC	Quantum Confinement
ROS	Reactive Oxygen Species
SARS-CoV	Severe Acute Respiratory Syndrome Coronavirus
SARS-CoV-2	Severe Acute Respiratory Syndrome Coronavirus-2
SB	Spunbond
SCCM	Standard Cubic Centimeters Per Minute
SE	Secondary Electron
SEM	Scanning Electron Microscopy
XPS	X-ray Photoelectron Spectroscop

Chapter 1

Introduction

1.1. Motivation

Virus outbreaks can easily and rapidly spread around the globe with different modes of transmission, such as droplets, fomites, and aerosol. The most recent outbreak has happened due to the emergence of COVID-19, which has largely impacted our society, economy, and environment in addition to infecting more than 230 million people globally [1-3]. This new virus, SARS-CoV-2, is a new version of already emerged coronaviruses (e.g., SARS-CoV and MERS-CoV). Since the virus is viable in aerosols and on different surfaces for up to 7 days, symptoms of viral infection can result from continuous contact with contaminated surfaces, which can cause the transfer of the virus to facial mucosa [4, 5]. Personal protective equipment (PPE), especially face masks, has been shown to be effective in inhibiting transmission of virus from the environment to human body [6]. However, there are concerns with the use of conventional face masks, such as the long lifetime of viral particles on the face-mask surface and fomite transmission due to contamination and disposal of used face masks [7]. Incorporation of antiviral properties could prevent such infections by reducing the lifetime of SARS-CoV-2 and other viruses on the surfaces. In the past, various nanomaterials have been introduced as antiviral agents for different applications [8]. However, only after the emergence of COVID-19 have researchers shown a huge interest in nanomaterials to fight against viruses and a significant number of reports have been published on nanomaterials and coronavirus (see Figure 1.1).

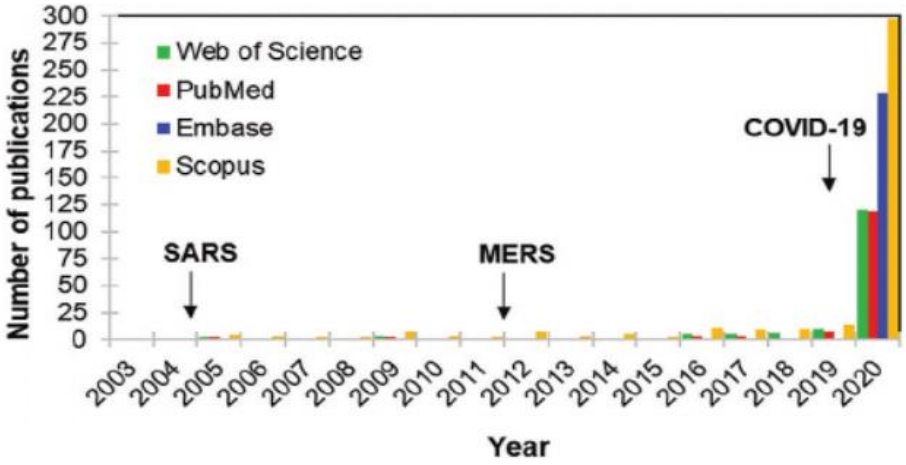

Figure 1.1. Publications shown on Web of Science, PubMed, Embase, and Scopus. Search words: "nano OR nanomaterials OR nanoparticle" and "coronavirus" [9].

Copper and its oxides are among those nanomaterials, which exhibit great antiviral performance, but they have been mostly deposited on rigid substrates [10-13]. Applications of functional textiles are undervalued and thus, there are limited reports on textile functionalization by metal-oxide incorporation. Cu/CuO_x nanomaterials are a promising agent to make antiviral fabrics, especially face masks, which could play a critical role in limiting the spread of the virus. Zinc oxide is another nanomaterial that can add multiple functionalities to textiles including self-cleaning, UV protection, and antimicrobial activity. Different liquid as well as vapor techniques have been utilized to incorporate these oxides into fabrics [14].

Applications of functional materials in textiles are still limited by challenges associated with technology, cost, and safety. Although copper has been approved by the US Environmental Protection Agency as a safe antimicrobial agent for use in human protection equipment, it still can be harmful, if a large amount is used and the coating has poor adhesion [15]. Furthermore, most technologies are designed for lab scale production, which makes the mass production very expensive.

Atmospheric-Pressure Spatial Atomic Layer Deposition (AP-SALD) is a technique that can address the challenges mentioned above by high-throughput, conformal deposition of coatings with thickness control as thin as the monolayer (atomic) level.

1.2. Thesis Overview

The main objective of this thesis work is to demonstrate the coating of fabrics with metal oxides, especially, Cu_2O and ZnO, by AP-SALD that can be used for the functionalization of textiles. The adhesion of the coatings is tested by applying different mechanical tests on the coated spun-bond polypropylene (PP) fabric. Filtration tests are also performed to ensure that the coatings do not affect the filtration performance of the fabric. Furthermore, the growth rates of the coatings on the PP fabrics are studied by applying an in-situ virtual interface (VI) model. Lastly, the cytotoxicity of Cu_2O-coated PP is tested to ensure that they are safe for human use so that they can be utilized in fabrication of antiviral N95 respirators.

Chapter 2 of this thesis mainly focuses on literature review and summarizes the basic properties, especially antiviral properties for Cu_2O, applications, and techniques for the preparation of Cu_2O and ZnO. As the main synthesis technique for metal oxides in this work, the working principle and previous works of AP-SALD are described.

In Chapter 3, the AP-SALD apparatus in our lab and the working principles of the material characterization techniques used, such as Scanning Electron Microscopy (SEM), Ultraviolet-Visible (UV-Vis) Spectroscopy, and X-Ray Diffraction (XRD) are briefly explained. Moreover, the procedures of the mechanical tests (washing, linear abrasion, tape adhesion, twisting, and bending) to test the adhesion of coatings are described.

Chapters 4 and 5 present the results and discussion of this research. In Chapter 4, coating of Cu_2O and ZnO onto the spun-bond polypropylene fabric by AP-SALD is presented. The deposition parameters, characterization data and coating adhesion are discussed. Moreover, different approaches toward the measuring the coating thickness are presented and discussed. Chapter 5 explains the filter test on coated fabrics and presents the results along with necessary interpretation. Moreover, cell viability tests were performed for Cu_2O coatings for face mask applications.

Finally, in Chapter 6, conclusions for each chapter are presented and ideas for future work are provided.

Chapter 2

Literature Review

2.1. Copper oxide (CuO_x)

2.1.1. Basic Properties of CuO_x

Copper has two main stable oxides, which are cupric (CuO) and cuprous (Cu_2O) oxides. Cu_2O crystallizes in a cubic structure. In the structure, copper cations are in face-centered cubic (fcc) sublattice, and oxygen anions are in a body-centered cubic (bcc) sublattice. The copper atoms are linearly coordinated by two closest neighboring oxygens whereas oxygens are tetrahedrally coordinated by copper, as shown in Figure 2.1a. On the other hand, CuO has a crystal structure in the monoclinic centered lattice in which copper is coordinated by four oxygen atoms and vice versa (Figure 2.1b) [16]. Some crystallographic properties of CuO and Cu_2O are tabulated in Table 2.1 [17].

As well-known p-type semiconductors due to the presence of copper vacancies, the band gap values are generally in the range of 2.1-2.6 eV (2.17 eV in the bulk) for Cu_2O and 1.2-2.16 eV (1.2 eV in the bulk) for CuO. This means that Cu_2O can absorb light up to the visible region whereas CuO can absorb up to the near infrared (IR) region. Generally, nanostructures behave differently from the bulk. For example, the band gap can be tuned as a result of the quantum confinement (QC) effect by changing the grain size [18]. Other factors, such as doping and temperature, can also alter the band gap of these oxides.

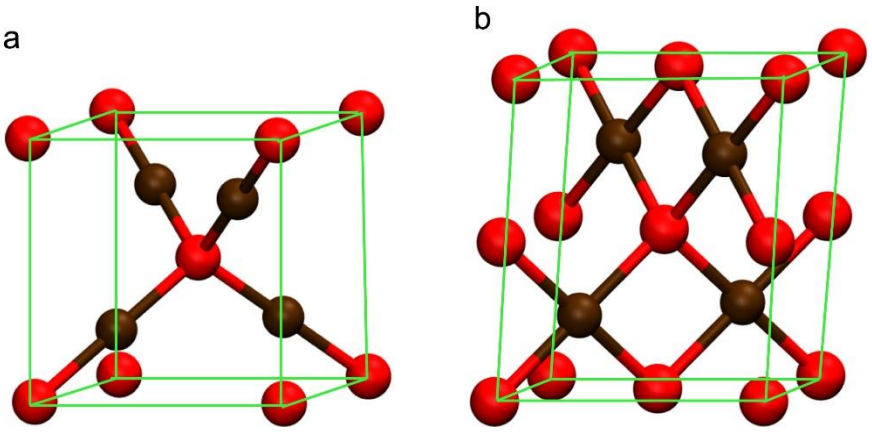

Figure 2.1. Crystal structures of (a) cubic Cu_2O and (b) monoclinic CuO (red and brown spheres represent copper and oxygen, respectively). Reprinted figure with permission from (Gattinoni et.al. 2015) Surface Science Reports

The electrical conductivity and hole density depend on the copper-vacancy density of CuO_x films. It has been shown that the conductivity increases as the temperature increases due to the increase in hole concentration. In addition, electrical properties of CuO_x also rely on grain sizes, film thickness, grain boundaries, and dopants [17].

CuO_x is used in various applications ranging from optical devices to antimicrobial systems due to its non-toxicity, low-fabrication cost, abundance of the constitutive elements, and unique properties [17, 19-21]. It has also played an important role in healthcare since ancient times, which will be explained in detail later in the chapter.

Table 2.1. Crystallographic parameters of Cu_2O and CuO [17].

	Space group	Lattice	Formula weight	Density	Melting Point	Cell volume
Cu_2O	O_h^4 or $Pn\bar{3}m$	Cubic a = 4.2696 Å	143.14	5.75 g cm^{-3}	1235 °C	77.83 $Å^3$
CuO	$C2/c$	Monoclinic a = 4.6837 Å b = 3.4226 Å c = 5.1288 Å β = 99.54° α = γ = 90°	79.57	6.52 g cm^{-3}	1201 °C	81.08 $Å^3$

2.1.2. Antiviral Properties of CuO_x

Copper has been known for its medicinal applications for thousands of years. Due to its low-cost, eco-friendliness, and biocompatibility, copper has been used for many different purposes, including sterilization, treatment of wounds, skin irritation, sore throats, eye infections, ulcers, and virus inactivation [22]. Similarly, its oxides have also been proven to have antiviral properties against several viruses, such as bacteriophages, human immunodeficiency virus (HIV), influenza virus, and coronavirus [23]. Humanity is facing challenges with new types of viruses every few years, which threaten human health and can cause pandemics, with the most recent being COVID-19. Severe acute respiratory syndrome coronavirus-2 (SARS-CoV-2), the virus that causes COVID-19, has an extremely high transmissibility and diffusivity due to the presence of asymptomatic carriers. With the emergence of COVID-19, Cu and its oxides received more attention to minimize the spread of the virus. The virus can survive up to 7 days on many surfaces, including stainless steel, plastics, and face mask surfaces [24], but Cu/CuO_x can reduce this time down to an hour, even less than an hour. For example, recently, it was shown that both CuO and Cu_2O effectively inactivate 99.9% of

SARS-CoV-2 in 1 hour when they were applied to door handles, pens, shopping cart handles, and card reader buttons, which are among the most touched objects in the public places [25]. Some examples of common-touch surfaces coated with CuO_x are presented in Figure 2.2.

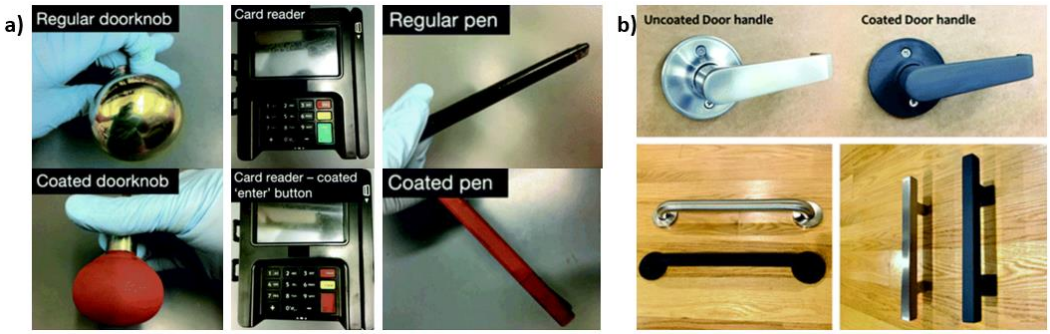

Figure 2.2. (a) Examples of different common-touch items coated with a Cu_2O/polyurethane coating. (b) Door handles coated with CuO (The figure (a) has been reproduced from ref. 10 and the figure (b) from ref. 11 with permission from the American Chemical Society).

Although the exact virus inactivation mechanism is unclear, it is proposed that the inactivation is related with the release of copper ions and the formation of reactive oxygen species (ROS). In recent work from our group, both Cu and Cu_2O coatings demonstrated strong virucidal effects against coronavirus 229E, a surrogate model for SARS-CoV-2, and the virucidal activity was enhanced in some cases due to the delamination and accelerated dissolution of Cu films in the viral droplets [13].

Released Cu^{2+} ions can oxidize the cysteine residues (RSH) to form RSSR or $Cu(SR)_2$ complex. Cu^{2+} can also inactivate double-stranded DNA (dsDNA) viruses by degrading the helical structure due to its interaction with viral nucleic acids. Cu^{+} interacts with cysteine amino acids by reacting with thiol (SH) and amine (NH_2) groups of cysteine residues. Cu^{+} also leads to the formation of ROS, such as OH and O_2^-, which also inactivate the virus through oxidative disruption. First, Cu^{+} reduces O_2 to form Cu^{2+} and O_2^-, which reacts with water to generate H_2O_2. Then, the obtained H_2O_2 reacts with

Cu^{+} to form OH, which further reacts with cysteine, tryptophan, and tyrosine residues [26]. This proposed mechanism is illustrated in Figure 2.3.

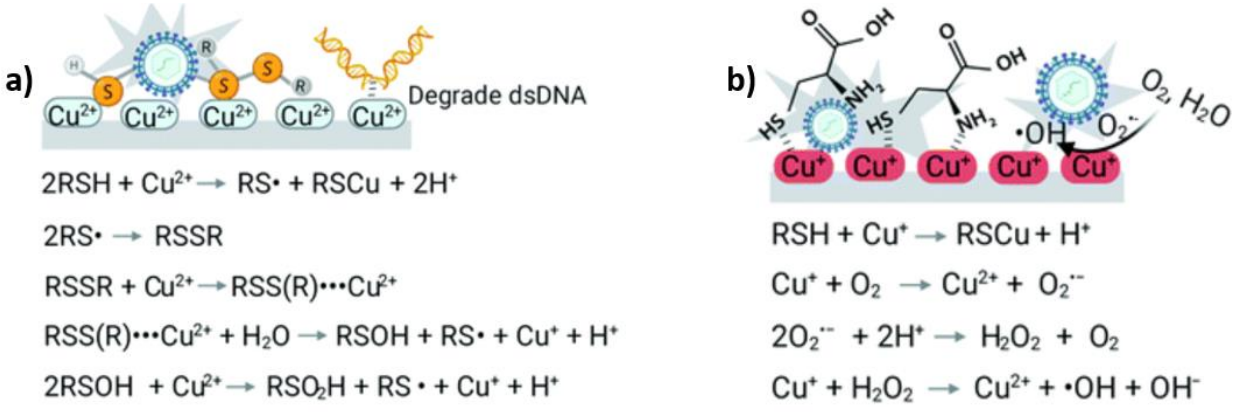

Figure 2.3. Virus inactivation on (a) CuO-coated and (b) Cu_2O-coated surfaces. Reproduced from ref. 26 with permission of Royal Society of Chemistry.

Although both cupric and cuprous compounds have antiviral properties, cuprous compounds have stronger antiviral activity than cupric compounds. For example, Cu_2O and Cu_2S reduced the viral titer by $10^{3.7}$-, $10^{3.2}$-, and $10^{5.8}$–10^{6} -fold for influenza A virus (H1N1), MS2 bacteriophage, and Qb bacteriophage, at 0.5, 2, and 5 h, respectively, while CuO and CuS reduced the viral titer only around $10^{0.01}$–$10^{0.59}$-fold. This difference suggests that Cu^{2+} ions have a lower activity during the virus inactivation [26].

2.2. Zinc Oxide (ZnO)

2.2.1. Basic Properties of ZnO

Another metal oxide semiconductor, which has been explored extensively is zinc oxide (ZnO). Depending on the conditions, ZnO can have three different crystal structures, which are wurtzite, zinc-blende, and rocksalt structures, which are shown in Figure 2.4 [27, 28]. The thermodynamically stable phase is wurtzite at ambient conditions. The rocksalt structure can be

formed at relatively high pressures, and the zinc blende structure can be obtained only on cubic substrates. In the wurtzite hexagonal structure, the lattice parameters are a= 3.25 Å and c= 5.21 Å. It is composed of two interpenetrating hexagonal-close-packed (hcp) sublattices of Zn and O. The zinc atoms are coordinated by four oxygen atoms making a tetrahedral coordination and vice versa [28].

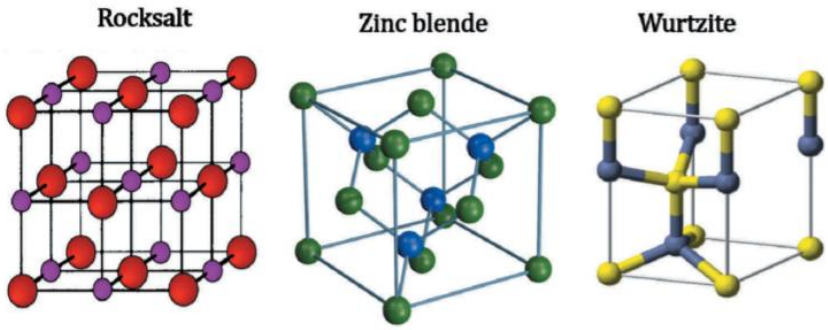

Figure 2.4. Different crystal structures of ZnO [27].

ZnO is a n-type transparent conductive oxide with a large direct band gap of 3.37 eV, which makes it transparent in the visible range of the electromagnetic spectrum [27]. In addition, it has a large exciton binding energy of 60 meV, which is larger than the exciton binding energy of many other wide-bandgap semiconductors such as GaN (25meV) and ZnSe (20meV) [28]. ZnO exhibits great photocatalytic activity, which is depicted in Figure 2.5 along with proposed mechanism. These exciting properties make ZnO a promising candidate for many applications, including optical devices, cosmetics, sensors, and medical devices.

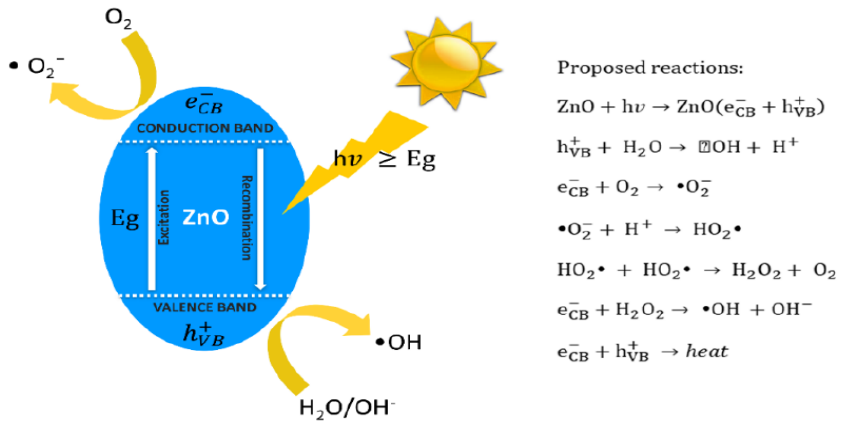

Figure 2.5. Proposed photocatalytic mechanism of ZnO [14].

2.2.2. Applications of ZnO-coated Textiles

Modification of textile surfaces is increasing in popularity as it can provide additional functions to common fabrics. ZnO is amongst the materials that can provide a wide range of functions, such as self-cleaning, UV protection, antibacterial activity, thermal insulation, moisture management, flame retardancy, electrical conductivity, and hydrophobic properties (Figure 2.6).

The photocatalytic activity of ZnO gives the fabrics capability of having self-cleaning properties. With this property, the fabric can decompose and remove organic dirt stains upon exposure to solar and UV light, without washing. In the photodegradation of stains, the reactive oxygen species (ROS) play an important role. Therefore, any factor that enhances the formation of ROS increases the photocatalytic performance. Higher ZnO concentration, surface porosity, hydrophilicity, roughness, and specific surface area are some examples that causes the formation of ROS, and thus increase in photocatalytic activity of fabric [14].

UV protection property of textiles is important, especially during the sunny summer days. By absorbing, refracting, or scattering the UV-A and UV-B radiation, textiles, especially those used in

clothing, block the UV light from reaching the skin. Binding agents, such as methacryloxypropyl trimethoxysilane and capping agents are used to enhance the adhesion of ZnO coatings [14].

With its high thermal stability, ZnO can also provide flame retardancy to textiles by reducing the heat, fuel and oxygen transfer between the flame and textile [14].

Another very common functionality that ZnO can provide to fabrics is antibacterial activity. Although the exact mechanism is not clear, it is known that antibacterial activity is attributed to ROS generation and Zn^{2+} ion release. Various textiles and synthetic fibers, including cellulose, polyester, polypropylene, polyamide, and polyurethane, have been coated with ZnO to test antibacterial activity against *Staphylococcus aureus* Gram-positive bacteria, *Escherichia coli* Gram-negative bacteria, Candida albicans, Bacillus subtilis, and many more. ZnO was one of the two candidates of this work as an antiviral agent, but previous work by Delumeau, Asgarimoghaddam and others showed that ZnO did not present any antiviral activity [13]. Being highly biocompatible, at least for low concentrations, ZnO is promising for the textile industry. However, high concentrations of ZnO in textiles can cause cytotoxicity. Therefore, controllable thickness of a ZnO coating is very crucial in these applications [14].

Figure 2.6. Schematic representation of functionalities that ZnO can add to textiles [14].

2.3. Preparation Methods For ZnO– and CuO_x – coated Textiles

Since there has been a great deal of interest in nanostructured metal oxides lately, different approaches have already been implemented in preparation of these oxides. Although most of the works have been done on rigid substrates, some studies have been conducted on textile functionalization with metal oxides. With their wide range of applications, CuO_x and ZnO nanostructures have been prepared on textiles with various liquid-phase as well as vapor-phase processes.

As the name suggests, liquid-phase techniques perform the synthesis in the liquid phase. Sol-gel, electrodeposition, and hydrothermal/solvothermal techniques are examples of liquid-phase techniques [14, 17]. The drawbacks of liquid-phase processes are that too many chemicals are used, which makes the waste treatment difficult and thus increases the cost. They are advantageous in terms of simple equipment operation and application for large-scale production. For example, Tencel Ltd., London, UK, deposits copper into cotton fiber by wet processing method, electroless

plating. They soak the fibers in $SnCl_2$ solution followed by $PdCl_2$ solution to obtain activated fibers. To get Cu (II) and Cu(I) containing fibers, they expose the activated fibers to formaldehyde, $CuSO_4$, and polyethylene glycol [22]. Ran et. al. utilized the hydrothermal method to coat cotton fabrics with ZnO as an example of a liquid-phase technique for ZnO growth on textiles [29]. In their work, they pre-treated the fabric surface using polydopamine (PDA) prepared by dissolving dopamine in a Tris buffer solution. Before growing the ZnO, they prepared a seed layer by immersing the PDA – templated cotton into the seed solution prepared from zinc acetate, methanol, and sodium hydroxide. After these steps, they immersed the fabric into the growth solution prepared by mixing zinc nitrate hexahydrate and hexamethylenetetramine. As seen in these examples, liquid-phase techniques may require multiple steps and chemicals to coat fabrics with metal oxides.

Alternatively, we can prepare CuO_x and ZnO nanostructures using vapor-phase processes, which can be divided into two main categories, physical vapor deposition (PVD) and chemical vapor deposition (CVD). PVD processes use physical forces to deposit films by sputtering or evaporating corresponding oxide or elemental Cu or Zn by applying laser irradiation, thermal heating, ion bombardment, or other ways [13,17, 30-32].

Among PVD techniques, sputtering, such as radio-frequency (RF) and direct-current (DC) sputtering, is common in the deposition of metal/metal-oxide thin films, including ZnO and Cu/CuO_x [32-34]. In a typical PVD process, a solid source material is exposed to energetic particles to eject the atoms. Generally, in the case of copper oxide deposition, the stoichiometry of the CuO_x can be controlled by varying the sputtering power. Low sputtering power ejects a smaller number of Cu atoms, which can effectively react with oxygen and form the oxide with higher oxygen content, CuO. On the other hand, a high sputtering power leads to the deposition of Cu_2O films and causes the presence of unreacted copper on the surface due to the sputtering of excessive Cu atoms [17]. Jung et. al. utilized DC magnetron sputtering to coat PP filters with Cu to use them in KF94 respirators [32]. They showed that the coatings are effective against SARS-CoV-2 virus and do not

affect the filtration efficiency of the face mask. However, the concern is that the oxygen ion-beam treatment of the fabric surface that is used to increase the adhesion of the coatings could reduce the static electricity in the mask, which may affect the filtration efficiency.

Another example of PVD is thermal evaporation. As its names suggests, deposition of a metal or metal oxide is performed by evaporating the material with heat in a vacuum or low-pressure environment. Recent work by our group tested the antiviral performance of various metal/metal oxides including Cu and Cu_2O [13]. Cu coatings were made by thermal evaporation on glass and PP fabric, and the Cu-coated glass was oxidized to Cu_2O by annealing at 225 °C. The temperature is essential to obtain the desired CuO_x thin films in this technique. Generally, Cu_2O is obtained at relatively lower temperatures compared to CuO. Apart from these methods, pulsed laser deposition (PLD) has also been used for the deposition of CuO_x and ZnO films. For example, Ramamurthy et. al. demonstrated the deposition of ZnO as well as CuO on nonwoven PP fabrics by PLD and studied the antibacterial activity [30]. They perform RF plasma etching on fabrics to enhance the adhesion of the coatings. Some of the reports about the coating of textiles with CuO_x and ZnO are summarized in Table 2.2.

Chemical Vapor Deposition (CVD) is a popular vapor-phase deposition process where the volatile reaction precursors react in the vapor phase or on the surface of a heated substrate to form desired thin films. CVD methods can make high-quality coatings with excellent conformality and cover flat as well as complex substrate surfaces [42]. Different variants of CVD, such as plasma-enhanced CVD, metal-organic CVD (MOCVD) and atomic layer deposition (ALD), have been developed. Herein, ALD will be explained briefly, as it will be compared with the AP-SALD technique used in this work.

Table 2.2. Selected works on coating of textiles with CuO_x and ZnO by various methods.

Textile Substrate	Metal Oxide	Preparation Method	Additional Treatment	Application	Ref
Polyester, polyamide	CuO	Cathodic cage plasma deposition	-	Novel technique demonstration	[35]
Cotton, polyester-cotton	CuO, ZnO	Sonochemical	-	Cytotoxicity study	[36]
Cotton, polyester, latex	CuO/Cu_2O	Electroless plating	-	Antimicrobial activity	[37]
Polypropylene	Cu	Spray coating	Shellac for the adhesion and hydrophobicity enhancement	Self-cleaning, Photoactive, antibacterial activity	[31]
Polypropylene	Cu	Thermal evaporation	-	Antiviral activity	[13]
Cotton	ZnO	In-situ sol-gel	-	Antibacterial activity	[38]
Cotton	ZnO	In-situ dip-coating	Hexamethyltrieth ylenetetramine for ZnO preparation	Antibacterial activity, UV protection	[39]
Polypropylene, Cotton	CuO, ZnO	Pulsed laser deposition (PLD)	RF plasma treatment for adhesion enhancement	Antimicrobial activity	[30]
Polyamide 66	ZnO	Atomic layer deposition (ALD)	-	Photocatalytic and antibacterial activity	[40]
Cotton	ZnO	Atomic layer deposition (ALD)/ molecular layer deposition (MLD)	Al_2O_3 seed layer deposition	Electrical conductivity	[41]

ALD is a sub-class of the CVD that provides conformal coating using sequential, self-limiting surface reactions. As illustrated in Figure 2.7, the ALD process consists of four consecutive steps: (1) the

first gaseous precursor ("Reactant A") is flowed into the reactor and chemisorbs on the substrate surface; (2) the reactor is purged with inert gas to remove unreacted precursor and by-products; (3) the second precursor ("Reactant B") is flowed, which reacts with first precursor on the substrate surface; (4) similar to step 2, inert gas is purged to get rid of unreacted precursor [43]. These four steps result in the formation of one atomic layer (monolayer) of the desired material and can be repeated to produce a film with a desired thickness. The four steps are for a process with two precursors that form a binary compound. However, it is also possible to prepare ternary or quaternary thin films using additional precursors.

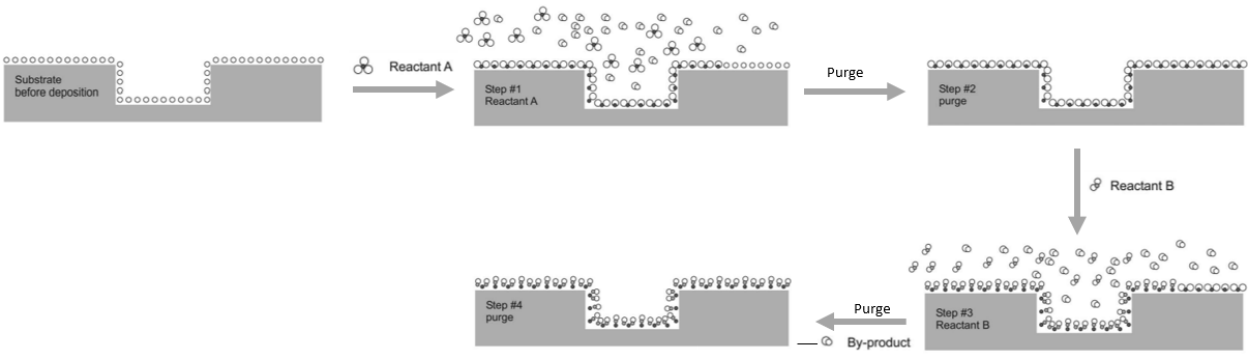

Figure 2.7. Schematic illustration of one ALD reaction cycle. Reproduced from ref. 43 with permission of Journal of Applied Physics

ALD has distinctive advantages, such as thickness control at the monolayer level, which can be controlled by the number of ALD cycles. Generally, the rate of the film deposition is described as *growth per cycle* (GPC), which is the thickness of material deposited on the surface by each 4-step ALD cycle. Limited work has been conducted on the coating of textiles by ALD. Polyamide 66 fabrics were coated with ZnO by ALD to study their photocatalytic and antibacterial properties, but the growth rate was not reported [40]. Instead, it was confirmed by studying the growth rate on silicon wafers. Another work was to coat a cotton fabric with ZnO to study the electrical conductivity [41]. No growth rate was reported in this work either. Measuring the thickness of coatings on textiles is very difficult as the surface is not flat and rigid. This makes the coating of textiles challenging.

CVD and ALD are similar techniques with some distinct differences. The main difference is that precursors enter the reactor separately in ALD, which eliminates the gas-phase reactions. Both techniques have some drawbacks, such as, precursors must be volatile at low temperatures and chemically stable; the substrate choice is limited; the reaction conditions can be complex, such as the need for a vacuum chamber; and film growth is slow [43].

It is well-known that Cu/CuO_x coatings can have poor adhesion, whereas robust coating is very important for mass production, especially in the textile industry since many textiles are washed. For this reason, additional steps have been taken to improve the adhesion of the coatings. For example, Karmacharya et.al. reported photoactive antiviral face masks by applying shellac/copper nanoparticles to surgical face masks with spray-assisted technology [31]. A main reason for using shellac was to strengthen the adhesion of the copper coating. Moreover, other pre-treatments applied to fabrics are oxygen ion beam and RF plasma etching to increase the adhesion of coatings [30, 32]. These additional chemicals and steps increase the cost of the production.

2.4. Atmospheric Pressure Spatial Atomic Layer Deposition (AP-SALD)

2.4.1. Basic Principles

Atmospheric-Pressure Spatial Atomic Layer Deposition (AP-SALD) is an emerging approach to ALD. Unlike in conventional ALD, precursors flow simultaneously in AP-SALD and are separated in space rather than flowing separately in time. This approach eliminates the need for the slow purging steps that slows conventional ALD and the vacuum environment that limits the scalability of conventional ALD.

AP-SALD can reproduce the ALD cycle and self-limiting reactions by moving the substrate between the gaseous precursor zones, resulting in monolayer-by-monolayer film deposition and excellent conformal coverage of the substate. On the other hand, conventional ALD completes the same process by keeping the substrate static and delivering the precursors sequentially in time [44].

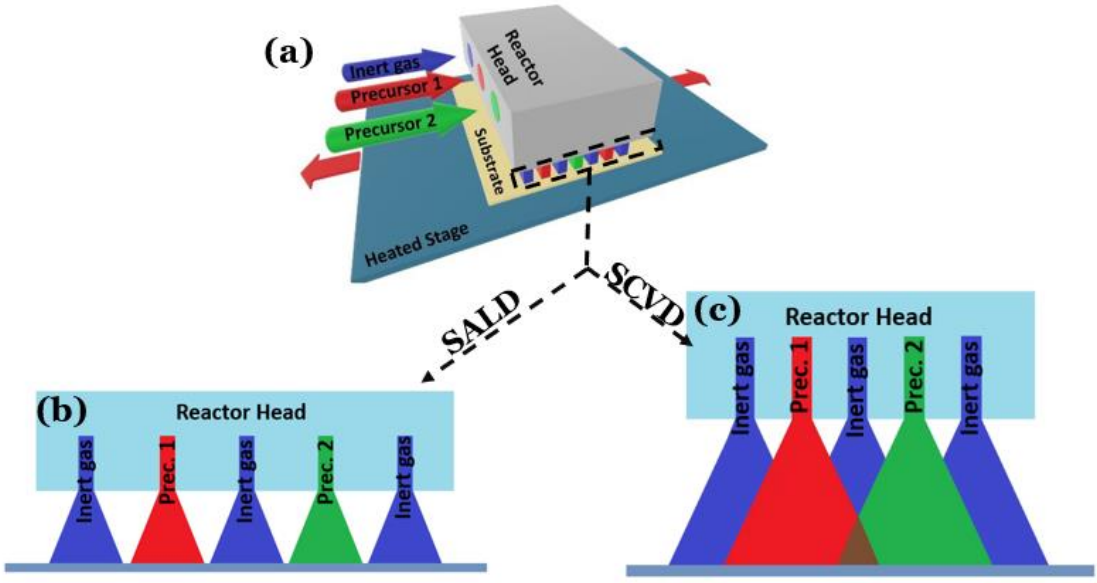

Figure 2.8. a) 3D drawing of reactor head in AP-SALD, which shows continuous flow of precursors. (b) Small gap between substrate and reactor head prevents mixing of the precursors in the gas phase whereas (c) large gap behaves like CVD process due to the mixing of precursors before reaching the substrate.

In AP-SALD, the component where the precursors and inert gas are separated as parallel flows and delivered to the substrate is commonly called the "Reactor Head" (Figure 2.8a). As this approach eliminates the vacuum process and purge steps of conventional ALD and the growth rate depends on the substrate oscillation speed, the film deposition rate becomes significantly faster compared to that of a conventional ALD system. Moreover, a main advantage of AP-SALD, especially for industrial applications, is its operability under atmospheric pressure, which removes the substrate size constraint making it compatible with commercialization. Keeping the small gap between the substrate and the bottom of the reactor head enables the deposition under atmospheric pressure

because a small gap ensures that the precursors reach the substrate without mixing in the gas-phase (Figure 2.8b). As the gap gets larger, the process starts behaving like a CVD process where precursors are directed into the chamber simultaneously and allowed to mix (Figure 2.8c). As a result, the precursors react in the gas phase before they reach the substrate. Generally, CVD exhibits a higher deposition rate compared to ALD (up to 2 orders of magnitude), but lower control over the thickness than the ALD process.

The film deposition in AP-SALD depends on many factors, such as the substrate temperature, oscillation speed, gap between the substrate and reactor head, flow rates of the gases, and sequence of channels in the reactor head.

2.4.2. CuO_x and ZnO Thin Film Deposition on Rigid Substrates

Although ZnO films have been deposited on various rigid substrates by AP-SALD and studied [45-47], there has been limited work on the deposition of CuO_x thin films by AP-SALD. Common metal precursors used for CuO_x and ZnO are Cupraselect and Diethyl Zinc (DEZ), respectively. Cupraselect favors the deposition of Cu_2O rather than CuO at lower temperatures (< 350 °C), but it can be controlled by varying the deposition parameters, especially the substrate temperature. As an oxygen source, the common precursor is water, and oxygen plasma and ozone are alternatives. According to previous reports, ZnO has a significantly higher growth rate (1.01 nm/ALD cycle) compared to Cu_2O (0.03 nm/ALD cycle), indicating that ZnO is readily deposited under SCVD conditions with an AP-SALD system. Selected reports have been tabulated in Table 2.3.

Doping can be achieved easily in AP-SALD by adding precursors to different channels. For example, Hoye et.al. has successfully made Mg-doped ZnO, which results in a bandgap change from 3.3 eV to 5.5 eV, depending on the Mg content [50]. Moreover, Illiberi et.al. demonstrated the deposition of

Al-doped ZnO films resulting in a high carrier density, low resistivity as well as more than 85% optical transparency in the visible region [51]. Similar effects can be seen in CuO_x films by doping the film with nitrogen [52] and some cations, such as Sn^{2+} and La^{3+} based on the theoretical calculations [53].

Table 2.3. Selected works on Cu_2O and ZnO films by AP-SALD

Material	Precursors	Oxidant	Growth Rate (nm/ALD cycle)	T (°C)	Application	Ref
Cu_2O	Cupraselect	Water	0.025	150-225	Solar Cells	[48]
Cu_2O	Cu(hfac)(cod)	Water	0.016-0.052	180-260	Solar cells	[49]
ZnO	DEZ	Water	0.05-1.01	50-200	-	[47]
N-doped ZnO	DEZ + NH_3	Water	0.17	200	Thin Film Transistors	[46]

Other deposition parameters, such as deposition temperature, can also be varied to tune the properties of the film. For example, Sekkat et. al. showed that the bandgap of Cu_2O films can be varied between 2.08 eV and 2.5 eV using different deposition temperatures [49].

Since the properties of these films can be tuned depending on the intended use, they have been used in many different applications, such as solar cells, light emitting diodes (LEDs), and transparent conductors [44].

Despite these advantages of AP-SALD, it is worth noting the challenges and limitations of this technique. Generally, metal oxides have been deposited by AP-SALD. The non-oxide films are uncommon because exposure of films to atmosphere could negatively affect the film properties because of oxygen incorporation into the films. Trying to avoid this adds complexity to the system, which increases the cost and limits its use. Moreover, flow channels are prone to blockages as

deposition can occur in the channel before the precursors reach the substrate. Furthermore, variations in the gap spacing between the reactor head and the substrate can cause non-uniform film deposition. Hence, careful control of all AP-SALD system parameters is essential. For some precursors, such as Cupraselect, heating is required because of their low vapor pressure, which adds further complexity to the system.

Chapter 3

Experimental Techniques

3.1. Description of SALD System at UW

The depositions of this work have been done using an AP-SALD system, which was designed and developed in our lab. One main part of this system is a gas delivery system, which includes valves, precursor bubblers, and mass flow controllers (MFCs). Figure 3.1 shows a simple schematic of the gas delivery system of our SALD technique. The precursors are stored in bubblers in either liquid or solid form, depending on the precursor, and kept at room temperature. However, in some cases, like the Cu_2O deposition in this work, the precursor bubbler may need to be heated due to the low vapor pressure of the precursor. Gaseous precursors are carried by bubbling inert gas, nitrogen, through the precursors, whose flow is controlled by MFCs. Then, there is another nitrogen flow added to the line, which is typically used to adjust the precursor concentration before reaching the reactor head and substrate. It is also possible to purge the lines without flowing through the bubblers (to remove chemical precursors from the gas lines) by opening a purging line valve located immediately downstream of the bubblers. All the flowing gases are delivered to the component called “Reactor Head”, which is made from a stainless-steel block. By flowing through the reactor head, each precursor is directed to the separate slits, which are placed parallel to each other facing down towards a heated substrate stage that oscillates back and forth at certain speed.

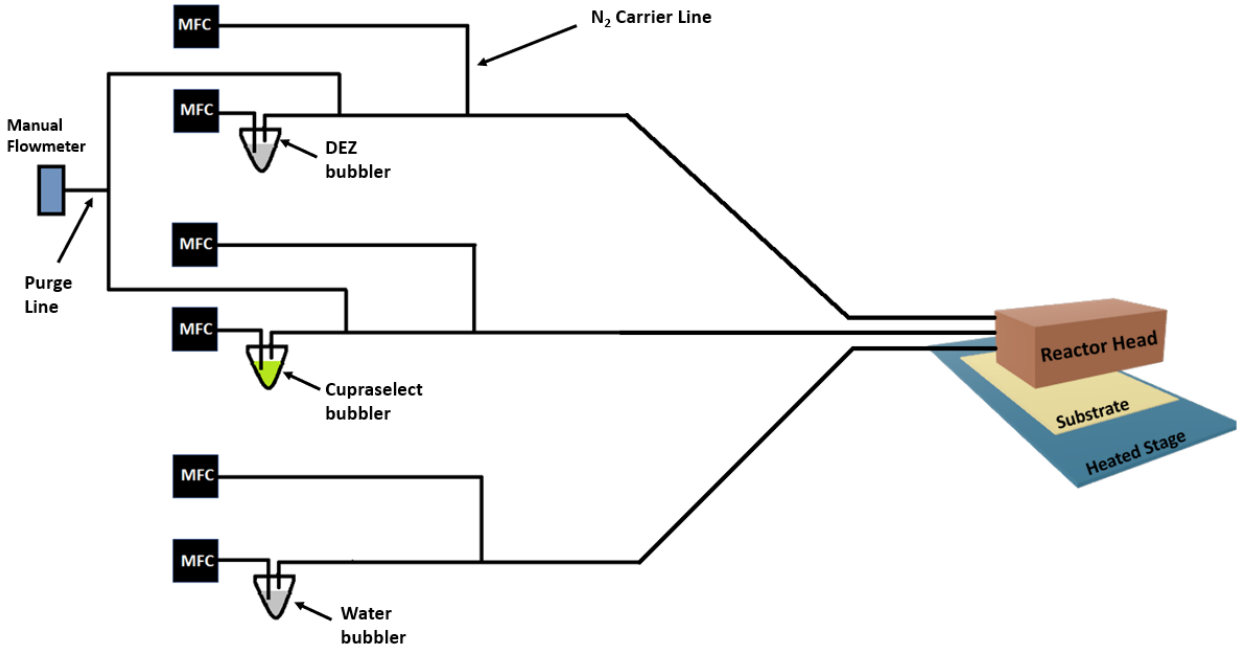

Figure 3.1. A schematic representation of gas delivery system of SALD in our lab

The reactor head has 4 inlets, one for nitrogen gas, one for an oxidant, and two for metal precursors, or one metal and one catalyst or dopant depending on the desired deposition composition. The outlet is divided into 21 thin slits through which precursors are delivered to the substrate separately in specific arrangement (Figure 3.2). The role of nitrogen gas between each reactant slit is to separate the gases and minimize their contact with the atmosphere. Furthermore, the nitrogen flow removes the unreacted precursors from the substrate. There are also exhaust slits available (shown in figure 3.2) to pull the unreacted and unnecessary reactants out by suction. With this configuration, a substrate exposes to precursor twice (since Metal 1 line is used for both CuO_x and ZnO precursors) in 1 full AP-SALD oscillation and thus, consists of 2 ALD cycles. This is one advantage of AP-SALD over conventional ALD that allows faster deposition.

In the ALD process, the two half-reactions on the substrate surface need to reach equilibrium, which requires sufficient precursor concentration in the outlets of the reactor head, nitrogen flow with sufficient rate, and enough interaction time between the precursor and the substrate. The first

two requirements can be satisfied by tuning the flow rates and the last one by adjusting the oscillation speed of the substrate. However, saturation depositions must be performed before running the actual deposition every time the system is started to make sure the line is saturated, and the precursor concentration stabilizes at the reactor head outlet. The time required to reach the saturation depends on the system and the precursor being used. For zinc and copper precursors in the system I used, the saturation time is less than 20 and 30 minutes, respectively.

With the lab-scale AP-SALD system, a maximum area of 7 cm x 5 cm can be deposited. The stage can be heated up to ~500 °C, but only low temperatures (<200 °C) were used in this work due to the low melting point of the substrate used. The substrate oscillation speed can be as high as 300 mm/s, but most of the depositions were done at 50 mm/s or lower in this thesis. As discussed in Section 2.4, the gap between the reactor head and the substrate is very important and is manually adjusted using three micrometers.

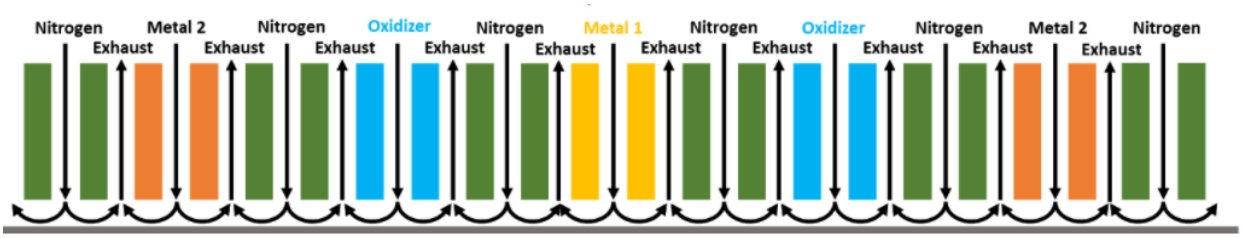

Figure 3.2. Distribution of precursors to separate slits on the reactor head.

3.2. Characterization Techniques

3.2.1. X-Ray Diffraction

X-Ray Diffraction (XRD) is an analytical technique that is used for phase identification and analysis of crystal structure. Generally, XRD patterns are interpreted with “Bragg’s Law”, which is defined as:

$$n\lambda = 2d\ sin\theta \tag{3.1}$$

where n is an integer, λ is the wavelength of the X-Ray beam, d is the distance between diffracting planes and θ is the incident angle as shown in Figure 3.3. In the process, X-Rays are generated by a cathode ray tube and hit the sample, which forms constructive interference and diffracted rays as long as Bragg's Law is satisfied. Then, diffracted rays are detected by the detector and converted to a count rate, which can be seen on the screen. All possible diffraction directions are scanned by running the measurement over the range of 2θ. Each crystalline substance has a unique XRD pattern depending on the crystal type, atomic size, and arrangement. In addition to phase identification and crystal structure analysis, it is also possible to analyze the crystal quality with XRD. The peak widths give information about the crystallinity of the sample. Sharper peaks are indicative of more crystalline samples (i.e., larger crystallite sizes) whereas crystallinity decreases as the peaks get broadened.

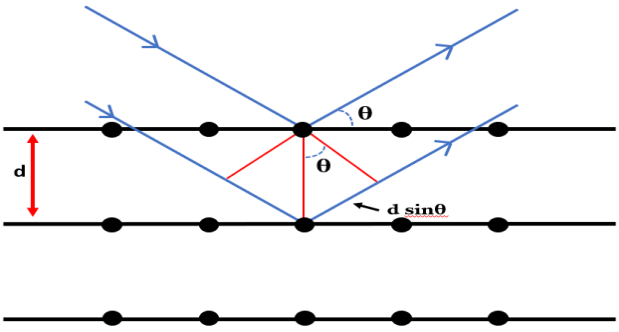

Figure 3.3. Schematic of Bragg's law.

In this thesis, Grazing Incidence XRD (GIXRD) was utilized for the analysis of thin films, as it limits the penetration of light into the bulk sample by using a small-incident-angle X-ray beam, and optimizes the intensity. All XRD patterns were collected on a PANalytical X'pert Pro MRD operating at 35 mA and 45 kV with a Cu anode (Kα = 1.5406 Å).

3.2.2. UV-Vis Spectroscopy

UV-Visible spectroscopy is used to analyze liquid as well as solid samples. To get the absorbance spectrum, absorbance of light at each wavelength (in the range of 200-900 nm) is measured, which excites the electrons in a sample from the ground state to an excited state. This spectroscopic technique relies on the "Beer-Lambert Law", which is defined as

$$A = \varepsilon bc \tag{3.2}$$

where A is absorbance, ε is the molar absorptivity, b is the path length, and c is the sample concentration. Many instruments use a monochromator to separate the light coming from the light source (typically, deuterium or tungsten lamp) into the individual wavelengths so that the spectrum can be recorded wavelength by wavelength. Some instruments use a diode array detector, which allows measurement of absorbances at all wavelengths simultaneously. This instrument is faster, more efficient, and eliminates the need of a monochromator.

It is possible to determine the bandgap of a semiconductor graphically by using a Tauc plot, which can be derived from a measured absorbance spectrum. The Tauc plot originates from Tauc's law, which can be represented by the following equation:

$$(\alpha h\nu)^{1/n} = B(h\nu - E_g) \tag{3.3}$$

Here α is absorption coefficient, h is Planck's constant (h = 6.62607004 × 10^{-34} m^2 kg / s), and ν is a frequency. B is another constant, E_g is the bandgap energy, and n is either 0.5 or 2 depending on the sample being analyzed. If the sample has a direct allowed bandgap, n is 0.5, and in the case of indirect allowed bandgap n would be taken as 2. From the equation above, $(\alpha h\nu)^{1/n}$ vs $h\nu$ would give a plot, which should have a linear region. When the linear region is extended to the x-axis, the x-intercept gives the optical band gap [54, 55].

In this thesis, a Horiba QuantaMaster 8000 spectrometer is utilized to obtain the UV-Vis spectra of the samples.

3.2.3. Scanning Electron Microscopy (SEM)

SEM is a vital technique to analyze the surface morphology and composition of nanomaterials. Due to their shorter wavelengths, which enables better resolution, electrons rather than light are accelerated in this technique. A high-energy electron beam hits the sample surface (depending on the accelerating voltage, it can penetrate to a depth of a few microns) and produces secondary electrons (SE), backscattered electrons (BSE), and characteristic X-rays. Secondary electrons are generally formed at lower depth and thus, have relatively low energy. They are good for imaging of surface morphology. On the other hand, back scattered electrons have high energy and reveal heavy elements, which backscatter electrons more strongly compared to light elements. Thus, BSE imaging is great for heavy elements since they have a bright appearance in the image. When the primary electron beam hits the sample, it can knock off an electron from the inner shell of atoms in the sample, which leaves a positive electron hole. To fill the vacancy, an electron from the outer shell moves to the inner shell releasing energy in the form of an X-ray. The energy of the X-ray is different for each element and thus can be used for element identification using energy dispersive X-ray spectroscopy (EDX) [56]. A summary of the electron-beam interaction is shown in Figure 3.4.

In this thesis, SEM and EDX were done either on a Zeiss LEO 1530 field or Zeiss Ultra Plus field emission SEM. Both secondary electron and back scattered electron modes were used for imaging the samples.

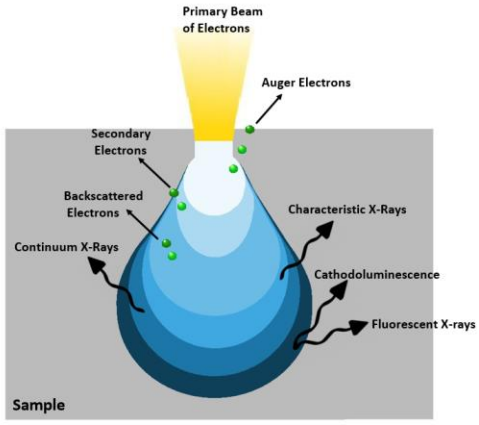

Figure 3.4. Electron beam interaction.

3.2.4. X-ray Photoelectron Spectroscopy

In this technique, X-rays with energy E_{photon} are directed to the sample surface where electrons absorb the radiation. When electrons absorb enough energy ($E_{binding}$), they are ejected with some kinetic energy ($E_{kinetic}$) and are analyzed by the detector (Figure 3.5). Elements are identified by their electrons' unique binding energies, which can be determined from the following equation:

$$E_{binding} = E_{photon} - E_{kinetic} - \varphi \tag{3.4}$$

where φ is the correction factor specific to the instrument. Since E_{photon} is known and $E_{kinetic}$ is measured by the detector, $E_{binding}$ can be calculated from the given equation. The binding energy is dependent on the shell where electron is located as well as its environment. Each element, except hydrogen and helium, has characteristic peaks, which makes chemical analysis possible. In this thesis, XPS measurements were performed using a multi-technique ultra-high vacuum Imaging XPS Microprobe system, Thermo VG Scientific ESCALab 250 and obtained data was analyzed with CasaXPS software.

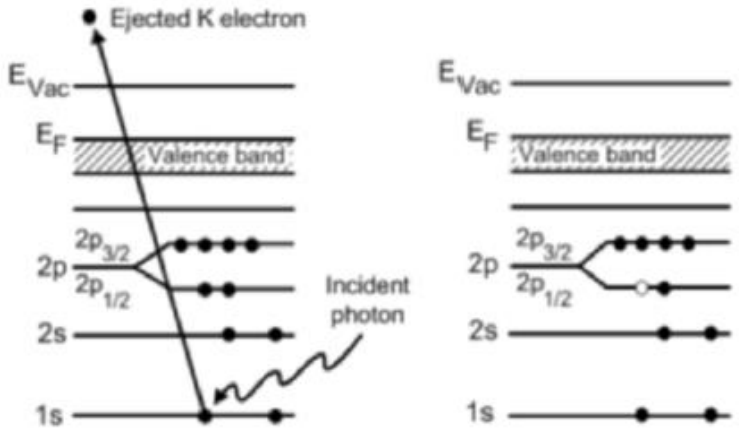

Figure 3.5. Initial (left) and final (right) state in atomic orbitals in XPS process. Reproduced from ref. 57 with permission of Springer Nature.

3.2.5. In-Situ Reflectance Spectroscopy

Reflectance spectroscopy is another type of spectroscopic technique, which measures the fraction of incident light reflected by the film surface as a function of wavelength. It is worth noting that reflectometry is an indirect technique, which means that it does not measure the film properties directly. Instead, a model-based approach must be used. The measured reflectance spectrum needs to be fitted to a modelled spectrum to analyze the film properties. Since the film deposition takes place in open air, there are two different interfaces, air-film and film-substrate. At the air-film interface, some part of light is reflected, and some transmits through and reaches the film-substrate interface where similar reflection and transmission occur. The Fresnel reflectance model is a suitable model to analyze the interaction of light with such interfaces with different optical media [58]. To apply the Fresnel model, optical properties, such as refractive index (n) and extinction coefficient (k) of the substrate must be known. In this work, since the substrate is a porous polypropylene fabric, it is hard to define accurate optical properties. Therefore, another reflectance model called the Virtual Interface (VI) model was used. The VI model was introduced by Breiland

and Killeen, who reported that there is no need for optical properties of the substrate to perform the measurement [59]. Unlike the Fresnel model, which fits the whole reflectance spectrum at a particular point in time, the VI model analyzes the reflectance at a single wavelength as a function of time, as shown in Figure 3.6.

In the VI model, the following equation is used to model the reflectance intensity at a specific wavelength as a function of time:

$$R(t) = \frac{R_\infty - 2\sqrt{R_\infty R_i}e^{-\gamma t}\cos(\delta t - \sigma - \varphi) + R_i e^{-2\gamma t}}{1 - 2\sqrt{R_\infty R_i}e^{-\gamma t}\cos(\delta t - \sigma + \varphi) + R_\infty R_i e^{-2\gamma t}} \tag{3.5}$$

where *R(t)* is a reflectance intensity as a function of time, σ is a phase of the internal complex reflectance, R_i and R_∞ are the reflectance of the substrate and infinitely thick film, respectively. Some of the terms in the Equation 3.5 belong to the oscillatory pattern; γ is a decay constant, δ is a frequency, and φ is a phase shift term. These terms can be defined by equations consisting of *n*, *k*, and another important term, growth rate, *G*, and substituting those equations into the Equation 3.5 makes the *R(t)* dependent on five unknowns, *n*, *k*, *G*, R_i, and σ. Since, *R(t)* forms a damped oscillatory pattern, initial values for the five unknowns can be estimated from the plot (Figure 3.6.) with the following equations:

$$R_\infty \cong \langle R(t) \rangle_t \tag{3.6}$$

$$\delta \cong \frac{\pi}{T} \tag{3.7}$$

$$\gamma \cong \frac{\ln\left(\frac{R_m}{R_{nm}}\right)}{T_m} \tag{3.8}$$

$$G \cong \frac{\lambda\delta}{4\pi}\left[\frac{1+R_\infty}{1-R_\infty} - \sqrt{\left(\frac{1+R_\infty}{1-R_\infty}\right)^2 - \frac{\gamma^2+\delta^2}{\delta^2}}\right] \tag{3.9}$$

$$n \cong \frac{\delta}{G} \tag{3.10}$$

$$k \cong \frac{\gamma}{G} \tag{3.11}$$

$$\sigma \cong tan^{-1}\left(\frac{-\frac{R'(0)}{\delta}}{R_\infty - R(0)}\right) \tag{3.12}$$

$$R_i = \frac{(R_\infty - R(0))^2 + \left(\frac{R'(0)}{\delta}\right)^2}{4R_\infty(1 - R_\infty)^2} \tag{3.13}$$

Finally, a nonlinear-least square fitting method such as the Levengberg-Marquardt algorithm is applied to determine the true *n*, *k*, and *G* values of the films.

In this thesis, an Ocean Optics QR600 reflectance probe, Ocean Optics DH-2000 UV-Vis light source, and Ocean Optics HDX-UV-VIS spectrometer with a range of 250 – 800 nm were used to perform in-situ reflectance measurements. The system captures reflectance data every two AP-SALD cycles at the same spot on the substrate.

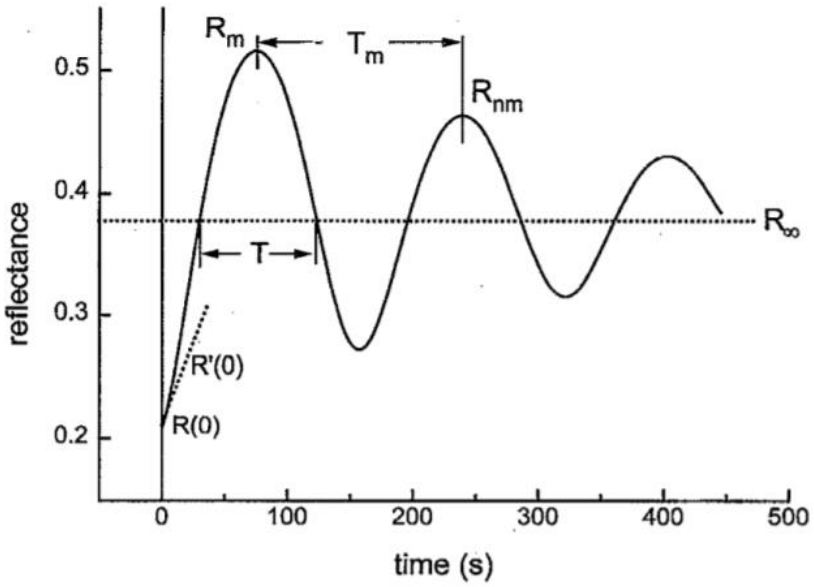

Figure 3.6. Reflectance vs time oscillatory pattern example and the unknowns that can be estimated as an initial guess. Adapted from ref. [59] with permission. Copyright 1995, AIP Publishing.

3.3. Mechanical (Robustness) Tests

Fabrics undergo different forms of mechanical impact (washing, rubbing, stretching) in applications, including clothing, gowns in hospitals, and even face masks. Thus, it is important that coatings are durable. Since we are proposing to coat outer layer of N95 respirators, removal of coatings may block the middle main filter (if not inhaled, which would have worse consequences) and thus, affect the filtration efficiency in case of poor adhesion. Moreover, if coating is peeled off after washing or applying external forces, such as rubbing, stretching, bending and/or twisting, it would lose its antiviral property in the removed regions, which is not practical. Thus, robustness analysis should be performed in every textile coating research. In this thesis, washing as well as other mechanical tests, such as linear abrasion, tape adhesion, twisting and bending tests have been performed to analyze the adhesion of the coatings when different external mechanical forces have been applied (Figure 3.7).

3.3.1. Washing

Coated fabric samples were washed with 200 mL water and 1.0 g of laundry detergent ("Gain" Original Liquid) with stirring (on "Torrey Pines Scientific" programmable stirring/hot plate HS61) at 450 rpm for 30 min at 40 °C. Then, the washed fabrics were rinsed twice within 200 mL of distilled water with stirring for 15 min to get rid of residual detergent particles. Finally, the fabrics were dried at 120 °C for 1 h on a hotplate in air.

3.3.2. Linear Abrasion Test

The fabric was placed face down on sandpaper (180 grit) with an object weighing 40 g on top of it, as shown in Figure 3.7a. The fabric was moved 10 cm along the ruler and then the same process was repeated 15 times. When pulling the fabric, the same angle of ~30° was used for reproducibility.

3.3.3. Twisting

In this test, one end of fabric was taped to the edge of a benchtop to keep it stationary, as shown in Figure 3.7b. The other end was twisted 360°. The twisting was done 50 times by twisting it in the opposite direction every time.

3.3.4. Tape Adhesion Test

The fabric was attached to the surface of a benchtop by taping both ends to keep it static, as shown in Figure 3.7c. Scotch tape was placed adhesive side down on the coated fabric and force was applied by putting 150 g of mass on it. The same mass was used every time to keep the applied force similar. The same process was repeated twice for each test.

3.3.5. Bending

In the bending test, the fabric was bent around a rod with radius of 4.5 mm, which was attached to a benchtop. The bending of the labeled same area was repeated 300 times, as shown in Figure 3.7d. The labeled bent region was analyzed by SEM to observe possible damages.

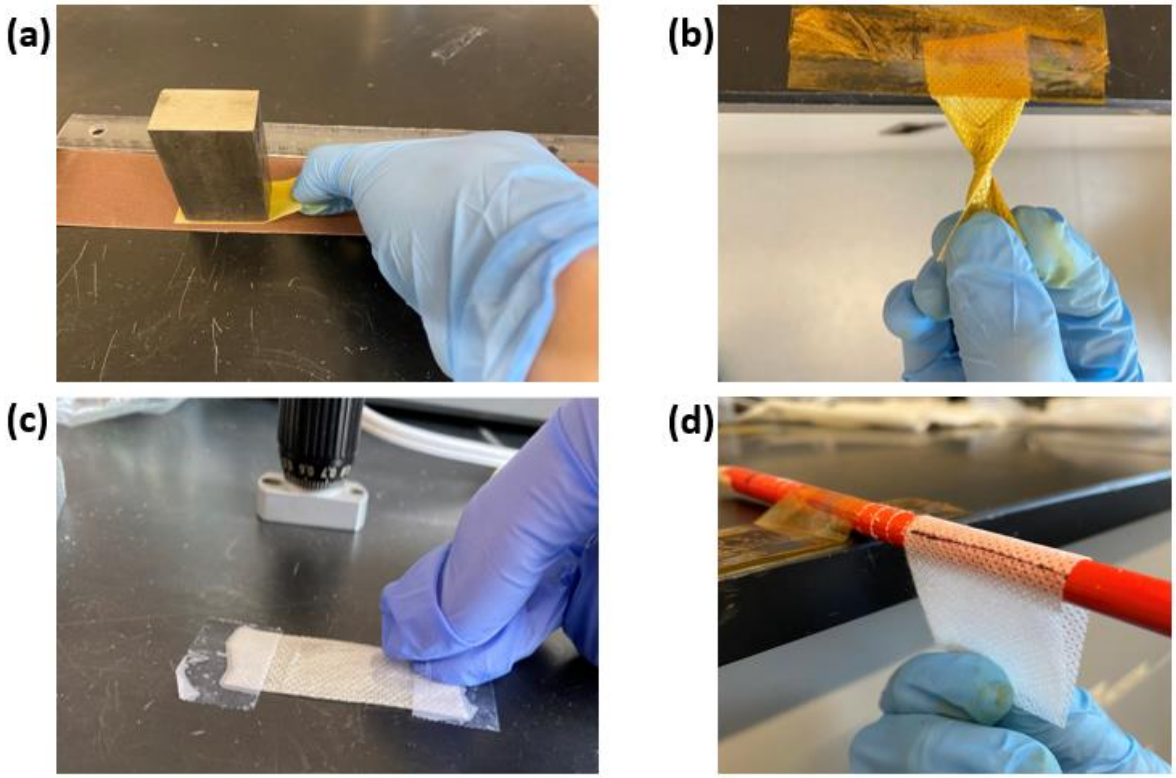

Figure 3.7. a) Linear abrasion, b) twisting, c) tape adhesion, and d) bending tests performed on the coated fabrics.

Chapter 4

Development of Robust Cu_2O – and ZnO – coated Polypropylene Fabrics by AP-SALD

4.1. Cu_2O – coated PP Fabrics

4.1.1. AP-SALD Precursors Used

Up to now, various copper precursors have been developed for the deposition of elemental copper and copper oxides (CuO_x) [48, 49, 60]. Copper(I) β-diketonate ($Cu^I\ (\beta - diketonate)L$) complexes are among the most widely used ones where L is a ligand that can be selected depending on the desired properties [61, 62]. For the deposition of Cu_2O thin films, the proposed general reaction mechanism is as follows:

$$Cu^I\ (\beta - diketonate)L_{ads} \rightarrow Cu^I\ (\beta - diketonate)_{ads} + L(g) \quad (4.1)$$

$$2\ Cu^I\ (\beta - diketonate)_{ads} + H_2O \rightarrow Cu_2O_{ads} + 2\ H(\beta - diketonate)(g) \quad (4.2)$$

In the first step of this reaction, the precursor is adsorbed onto the substrate surface where it decomposes due to the heat supplied to the substrate. After the decomposition, ligand L desorbs in the gaseous form and is purged with the nitrogen flow. In the presence of heat and water, the adsorbed species further decomposes to form gaseous $H(\beta - diketonate)$ leaving Cu_2O behind.

For this work, low fabrication temperature is crucial as the substrate (polypropylene fabric) melts at ~170 °C. Therefore, the chosen metal source needs to satisfy the temperature condition. Kang et. al. reported the deposition of Cu on Si wafers coated with PVD titanium nitride by thermal ALD at room temperature [63]. They used $Cu(hfac)_2$ (hfac = 1,1,1,5,5,5-hexafluoroacetylacetonate) as a

metal precursor (Figure 4.1a). They decreased the deposition temperature from 150 °C to room temperature by taking advantage of pyridine, which acts as a catalyst. In the proposed mechanism, the copper metal of $Cu(hfac)_2$ interacts strongly with pyridine on the substrate surface as copper is known to have strong interactions with Lewis bases. Moreover, there is hydrogen bonding between nitrogen lone pairs of pyridine and hydrogen of the hfac ligand. The proposed mechanism is depicted in Figure 4.1b. Both interactions are expected to weaken Cu – O bond, based on theoretical calculations [63].

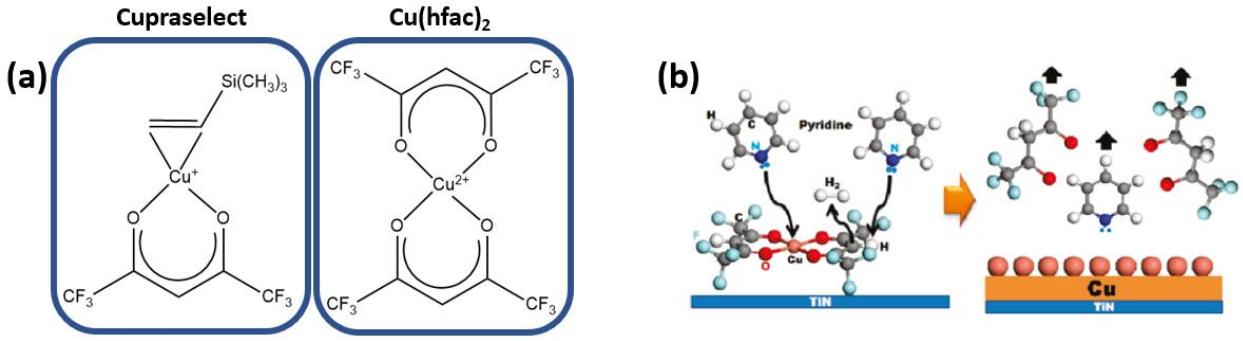

Figure 4.1. (a) Chemical structure of Cupraselect and $Cu(hfac)_2$. (b) Proposed mechanism of copper deposition. Reprinted with permission from ref. 63. Copyright 2010 American Chemical Society

Inspired by Kang and co-workers' report, $Cu(hfac)_2$ precursor was first studied in this work, as this precursor is less expensive than other precursors used in ALD and/or AP-SALD. In this precursor, both β-diketonate and ligand L are the same ligand, which is "hfac". One disadvantage of this precursor is that it is solid at room temperature and needs to be heated to form some vapor. During the deposition, the $Cu(hfac)_2$ bubbler temperature was set to 90 °C and the gas line was heated to 60 °C to reduce condensation in the line before it reaches the reactor head and substrate. Depositions were tried at different substrate temperatures from 150 °C up to 220 °C on borosilicate glass substrates. Inert nitrogen gas was flowed to carry the precursor vapors and ozone generated from an Absolute Ozone Atlas 30 UHC model ozone generator was used as an oxidant. The flow rate of pyridine was set to 50 sccm, which was diluted with 200 sccm of nitrogen carrier gas. The water

bubbler flow rate was 200 sccm, which also flowed through the $Cu(hfac)_2$ bubbler. It was diluted by 180 sccm of nitrogen carrier gas. Finally, the ozone production power was set to '75' to maintain the flow rate at ~650 sccm and separation nitrogen flow rates was set to 850 sccm. Film deposition was observed at 220 °C; however, the film was not uniform, and the deposition could not be consistently reproduced, either at similar conditions or many other experimental conditions tested.

By considering the possibility of having nucleation/adhesion problems for the copper precursor, the pyridine line was replaced with DEZ line to co-deposit ZnO as a dopant. The hypothesis here is that ZnO could help CuO_x to nucleate and deposit along with ZnO. In this approach, CuO_x/ZnO deposition was observed at a borosilicate glass substrate temperature of 210 °C with flow rates of 20 sccm (carrier gas at 150 sccm) for DEZ precursor, 200 sccm (carrier gas at 200 sccm) for water bubbler (which also flowed through the $Cu(hfac)_2$ bubbler), and 650 sccm for separation gas and ozone flow rates. The $Cu(hfac)_2$ bubbler and gas line were heated as mentioned above. However, the film deposition was again non-uniform. Deposition was observed only under the sides of the reactor head, or the deposited film was almost entirely ZnO without any CuO_x visible.

A second copper precursor, Cu(hfac)(TMVS) (TMVS = trimethylvinylsilane), which is also referred to as Cupraselect, was therefore tested for the deposition of CuO_x. In this precursor, β-diketonate is "hfac" again, but ligand L is TMVS (Figure 4.1a). AP-SALD of CuO_x with Cupraselect was studied previously [48], but it has never been used for deposition on fabrics. Cupraselect is a liquid with relatively low vapor pressure and thus, it was heated to 50 °C during the deposition. The low volatility may be because of its high molecular weight and strong intermolecular interactions. A disadvantage of Cupraselect is its thermally instability. Heating the bubbler enhances the decomposition of Cupraselect even if it is slow. As an oxygen source, water was used. Uniform CuO_x films were obtained by setting the flow rates for the bubbler and carrier gas to 450 and 50 sccm for Cupraselect and 200 and 300 sccm for water. The nitrogen flow was set to 1000 sccm and the gap between the reactor head and substrate was 100-150 μm. Uniform CuO_x films were obtained for

substrate temperatures ranging from 100 to 200 °C. The AP-SALD CuO_x films deposited using Cupraselect were first characterized on the borosilicate glass substrates and then on the PP fabrics.

4.1.2. Characterization of CuO_x Films on Glass

The deposition temperature is an important parameter in AP-SALD, especially for the deposition of CuO_x films. The composition of CuO_x film depends on the deposition temperature. Typically, Cu_2O forms at low temperatures whereas CuO forms at higher temperatures as a major phase [48, 64]. It was also noticed that the adhesion of the AP-SALD CuO_x films on glass increased with increasing deposition temperature. For example, there was a significant difference in adhesion for the CuO_x deposited at 150 °C and 120 °C. The latter could be easily wiped off the glass, whereas the CuO_x deposited at 150 °C could not be easily removed.

The optical properties of the films were determined by UV-Vis spectroscopy. Figure 4.2a shows the CuO_x thin films deposited at 100 °C, 120 °C, and 200 °C (500 AP-SALD cycles at 1.5 cm/sec oscillation speed) and Figure 4.2b and 4.2c show their absorbance spectra and corresponding Tauc plots (as described in Section 3.2.2). The direct allowed optical bandgap values for the films were calculated to be ~2.58 eV, suggesting the films are the higher-bandgap Cu_2O. Typically, bulk Cu_2O is known to have a bandgap value of ~2.1 eV. However, depending on the crystallinity and other characteristics of thin films, they can present different bandgap values. For example, Muñoz Rojas et. al. reported the bandgap value of Cu_2O thin films as 2.52 eV [48]. In another work, Sekkat et. al. showed that the bandgap changes with deposition temperature [49]. The calculated bandgap values are consistent with the literature value of Cu_2O thin films. Previous studies show that the bandgap depends on the morphology as well as crystallinity [65, 66]. The slightly higher bandgap observed for our films could be caused by a change in the point defects, which change the energy band structure.

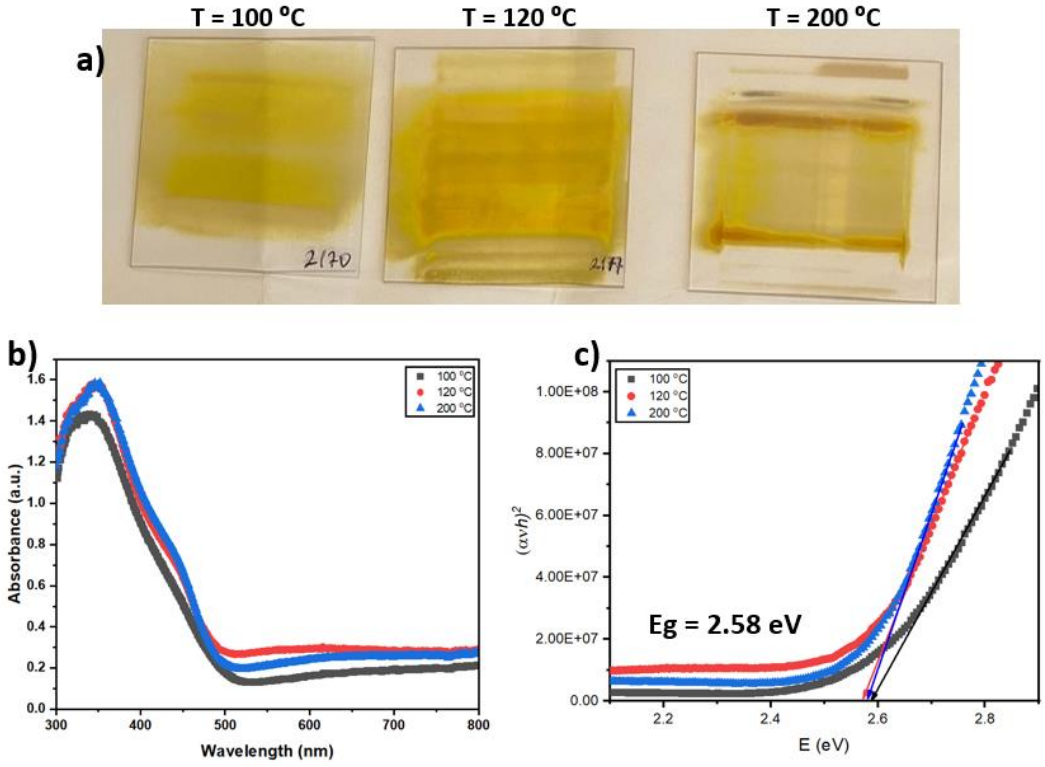

Figure 4.2. (a) The Cu_2O thin-film coatings deposited at 100 °C, 120 °C, and 200 °C, (b) their UV-Vis spectra, and (c) corresponding Tauc plots with calculated optical band gap energy values (E_g).

Figure 4.3 shows the XPS spectra for the surface of the Cu_2O samples deposited at 100 °C, 120 °C, and 200 °C. In the Cu 2p spectrum in Figure 4.3a, intense peaks corresponding to Cu 2p3/2 and Cu 2p1/2 at 932.5 eV and 952.2 eV, respectively, confirm that Cu_2O is the predominant phase in these films. There are also weak peaks at 933.4 eV and 953.2 eV corresponding to Cu 2p3/2 and Cu 2p1/2 of CuO, respectively. The presence of satellite peaks in Figure 4.3a is also an indicator that some CuO is present [67]. Unlike XRD, XPS performs analysis mainly on the surface and thus, the surface atoms may have oxidized to CuO due to the exposure to air, which could explain the presence of CuO peaks. Moreover, the O 1s spectrum in Figure 4.3b also suggests that the atomic concentration of oxygen atoms corresponding to Cu_2O (530.2 eV) is higher than that for CuO (531.5 eV).

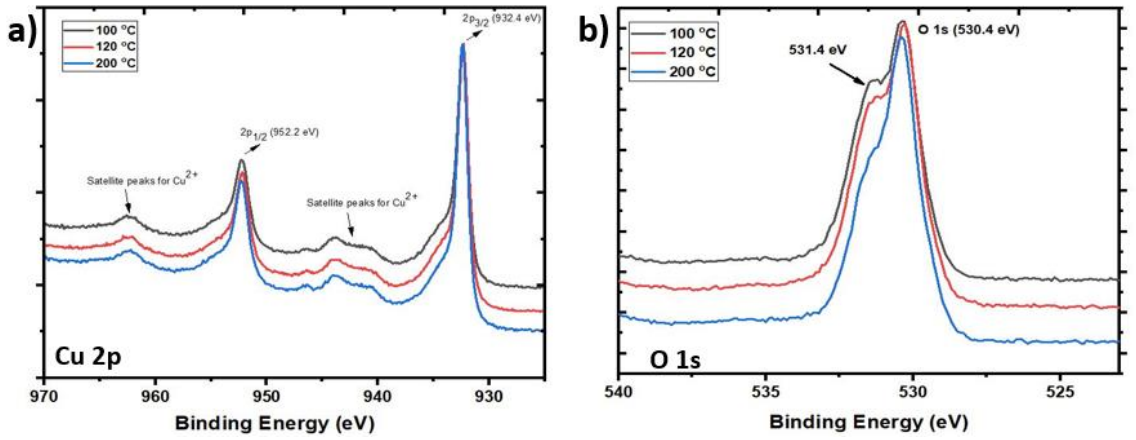

Figure 4.3. XPS measurement of Cu_2O samples showing (a) Cu 2p and (b) O 1s spectra.

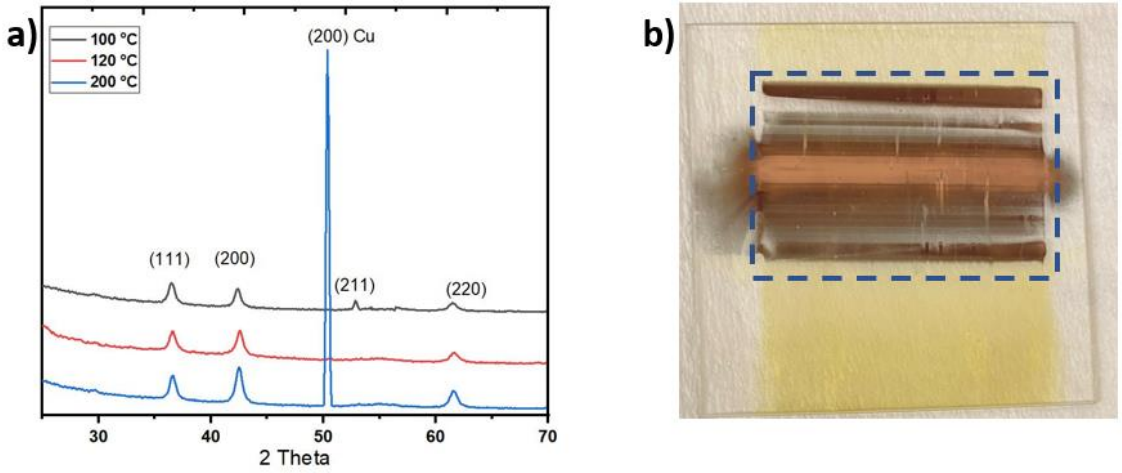

Figure 4.4. (a)XRD patterns of Cu_2O thin films deposited at 100 °C, 120 °C, and 200 °C. (b) Deposition of reddish-brown film at 200 °C (no oscillation)

XRD measurements of samples deposited at 100 °C, 120 °C, and 200 °C are shown in Figure 4.4a. Peaks corresponding to the (111), (200), and (220) planes of Cu_2O (JCPDS no. 05-0667) can be clearly observed for all samples. Hence, all three characterization techniques are consistent with each other and suggest that the Cu_2O is a major phase formed up to 200 °C. In the XRD pattern of the film deposited at 200 °C, there is a very strong peak at 50.5°, which does not belong to Cu_2O, but could be assigned to the (200) plane of elemental copper (JCPDS no. 04-0836). A possible

explanation for this is that Cupraselect decomposes at high temperatures [68]. Therefore, it might be decomposing at the higher substrate temperature to form elemental copper instead of the decomposition expected in the proposed mechanism. As shown in Figure 4.4b, the formation of a reddish-brown film was observed at 200 °C when the substrate was kept static (no oscillation), indicating that elemental copper is formed along with Cu_2O, which corroborates the XRD pattern. As 200 °C was not a suitable temperature in this work due to the low melting temperature of the substrate (PP), this precursor decomposition can be avoided.

4.1.3. Characterization of CuO_x Films on Polypropylene Fabric

Spun-bond polypropylene fabric (50 g/m^2), which is used as an outer layer of N95 respirators, was provided by Eclipse Automation Inc. and coated by AP-SALD. The fabrics were cut into rectangular pieces (8 cm x 7 cm) and attached onto the stage in tension by placing borosilicate glasses underneath to avoid the contamination of the stage. Depositions were performed by taping one, two, or three layers of spun-bond polypropylene fabric to the surface of the heated stage and setting the gap between the fabric and the reactor head to approximately 100-150 μm. Similar flow rates as those stated in Section 4.1.1 were used for the coating of fabrics. Polypropylene fabric has a melting point of 160-170 °C. For this reason, the deposition must be performed at low temperatures (less than 150 °C, as obvious damage has been observed on fabric at 150 °C). In this work, fabric depositions were performed at 100 °C and 120 °C.

It is worth noting that using textiles as substrates is more challenging compared to rigid substrates. Textiles are typically porous materials (spun-bond PP is one of them). As a result, some of the precursor can flow through the textile and may be wasted unless a proper solution is found. Figure 4.5a shows one layer of PP fabric (left), that was placed on top of glass (right) for a deposition of 500 AP-SALD oscillations (with oscillation rate of 1.5 cm/s). It is seen that in addition to coating the

fabric, there is significant deposition on the glass as well. To avoid that, two or three layers of fabric were taped onto the glass so that multiple layers of fabric could be coated at a time and deposition on glass is minimized (Figure 4.5b and c). It is clearly seen in Figure 4.5b and c that the precursor gas flows could pass through the upper fabric layer and reach the second or third layer; however, the different fabric layers were not coated equally. Simultaneous coating of multiple fabric layers with films of similar thickness may be possible by designing a custom reactor head compatible with fabrics, which contains exhaust slits under the fabrics so that the flow travels through the fabric layers more uniformly without hitting a rigid substrate underneath. This approach is proposed for future work at the end of this thesis.

It is also important that the fabric is held under appropriate tension to ensure a flat surface during deposition, otherwise non-uniform deposition can result. A sample of this issue is presented in Figure 4.6. As shown in the schematic in Figure 4.6a, two layers of fabric were placed on the glass for this particular deposition and at one location the fabrics did not sit flat on the substrate. Figures 4.6b-d show the top fabric, bottom fabric, and glass. Non-uniform coating is clearly observed. Minimal deposition is seen on the top fabric, indicating that most of the precursor gases passed through the top layer and reacted near the bottom layer of fabric and glass. The bottom layer of PP has a region with very little coating, which was located directly above a region on the glass with a thicker coating. As shown in the schematic in Figure 4.6a, when the fabric is not held under suitable tension during the deposition, the precursor gases can flow through it, become trapped in the region between the fabric and the glass and deposit on the glass. On the other hand, in the regions where the fabric is held close to the glass surface, the precursor doesn't have anywhere to go and thus, it gets trapped at the fabric-glass interface. This results in film deposition predominantly on the bottom fabric layer, as seen in Figure 4.6.

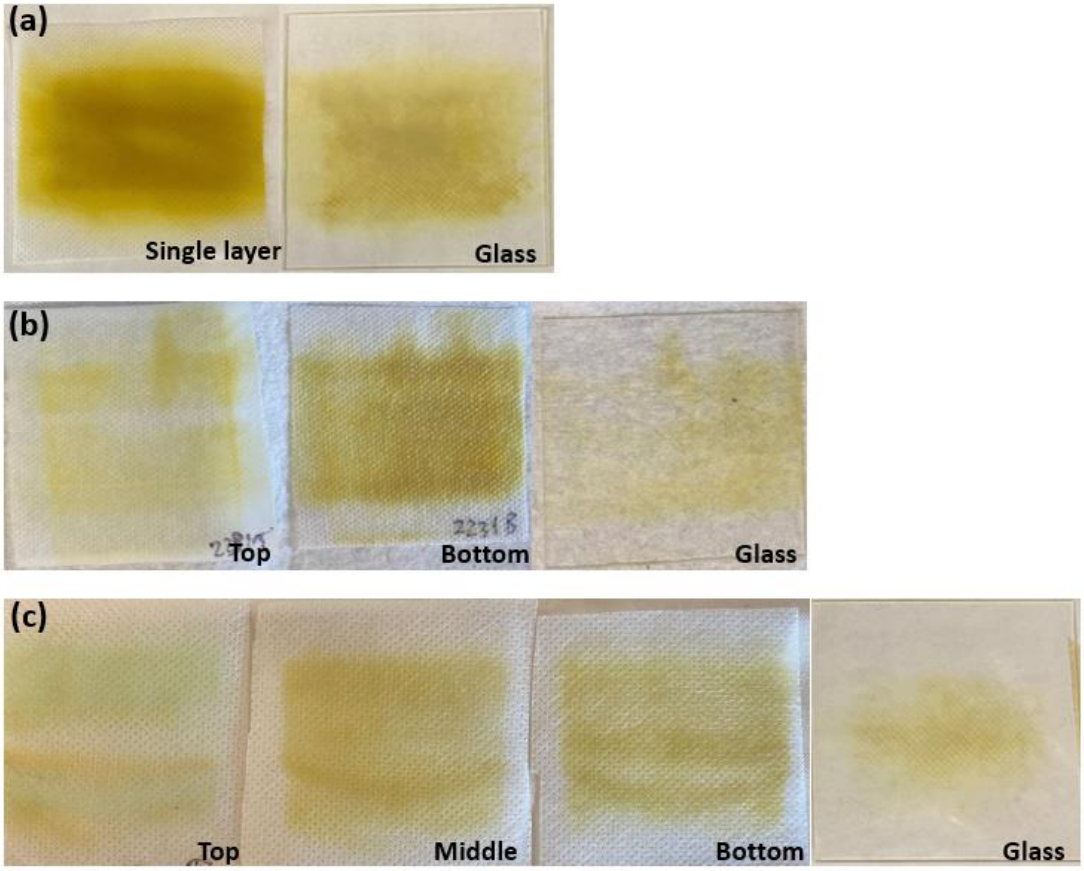

Figure 4.5. Coating of (a) one layer, (b) two layers, and (c) three layers of fabric on glass (7 cm x 7 cm) with Cu_2O.

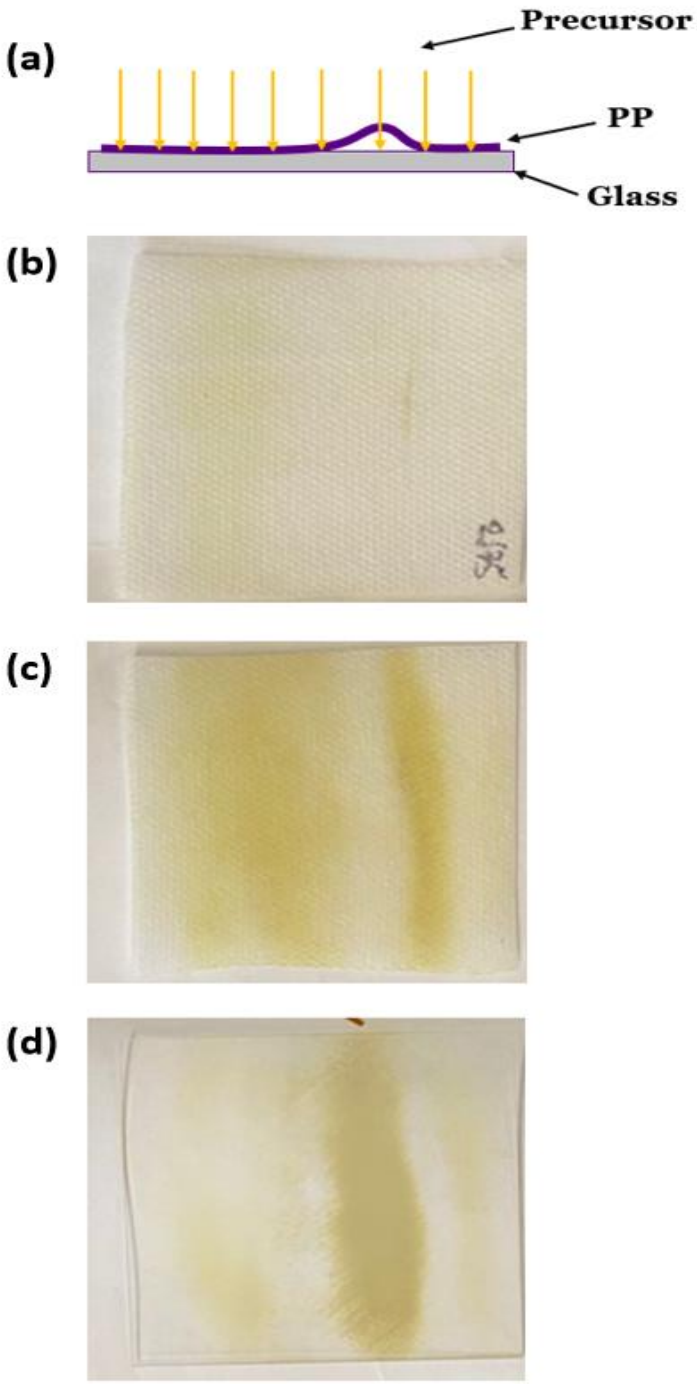

Figure 4.6. Example of non-uniform fabric deposition due to insufficient tension holding the fabric. (a) Diagram of experimental arrangement. Deposition on (b) top fabric, (c) bottom fabric, and (d) glass.

In this work, efforts were made to tape the fabrics to the stage with suitable tension to prevent any bunching of the fabrics and non-uniform deposition. In a roll-to-roll manufacturing process, the tension of the fabric would be controlled by the positioning of the rollers.

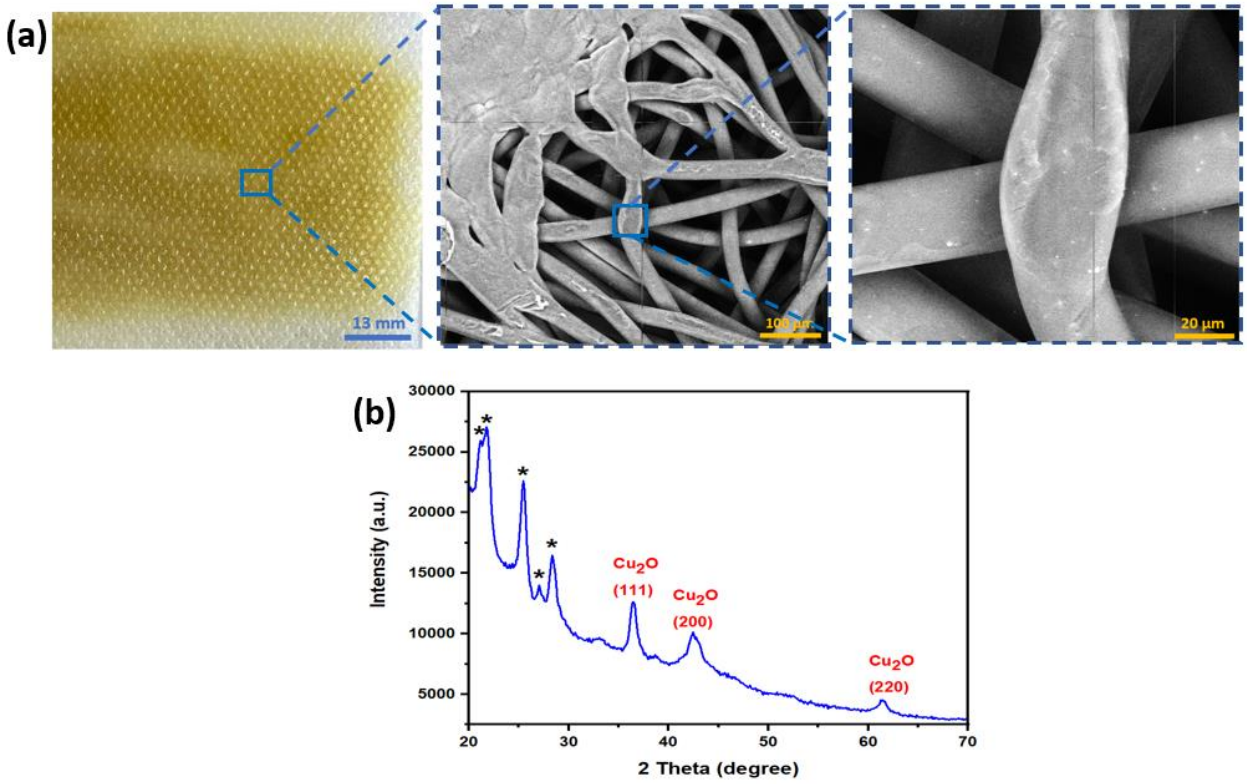

Figure 4.7. (a) Picture along with SEM images and (b) XRD data of PP fabric coated with Cu_2O at 120 °C. (Peaks labelled with "*" correspond to the PP).

Figure 4.7a shows the picture of one of the coated fabrics made at 120 °C using 500 AP-SALD oscillations and corresponding SEM images. The SEM images show that the Cu_2O conformally coats the fabric, forming continuous shells on the exterior of the PP fibers. Figure 4.7b shows the XRD measurement of the coated PP fabric. This data was collected from the bottom layer of a two-layer fabric deposition. The peaks in the spectrum belong to Cu_2O and PP only, which is consistent with the XRD data of the glass samples.

As mentioned earlier, thickness measurement of fabric coatings is challenging. Common techniques to measure the thickness, such as ellipsometry, interferometry, and stylus profilometer, are not suitable for fabrics [69]. It is common to see the reports in the literature in which growth rates of fabric coatings are estimated by determining the growth rate of a coating deposited at similar conditions on a silicon or glass substrate. However, this approach is not accurate as silicon and textiles have different morphologies and thus, will result in different growth behavior. In this work, different methods have been applied to measure the thickness of the Cu_2O coatings.

The first attempt was to analyze the cross section of a coated fabric with SEM imaging. It is important to have a clean cross section surface to get good-quality images. To do this, the coated fabrics were immersed into liquid nitrogen to make them brittle, cut into pieces and analyzed with SEM. However, this was not successful as it was found that the fibers plastically deformed when cut, despite the use of liquid nitrogen, as shown in Figure 4.8a. Another approach was to encapsulate the coated fabric with epoxy to make it rigid so that it would give a clean fracture surface when broken or cut into pieces. In this case, it was not rigid enough to break and thus, the epoxy-encased fabrics were cut into pieces and analyzed with SEM. The surface was coated with gold particles to avoid surface charging due to the fabric and epoxy being non-conductive. SEM images of one of the fabrics that was coated with Cu_2O at 120 °C using 600 AP-SALD oscillations is shown in Figure 4.8b. The images were much clearer than those from the previous approach. The coating is visible on the perimeter of the fiber as a change in contrast in the SEM image. The coating appears continuous and limited to the surface of the fiber; however, the achievable resolution does not permit accurate measurement of the coating thickness, presumably limited by the insulating nature of the PP fibers and epoxy. Finally, a VI model with in-situ reflectometry was applied to measure the thickness of the Cu_2O fabric coatings.

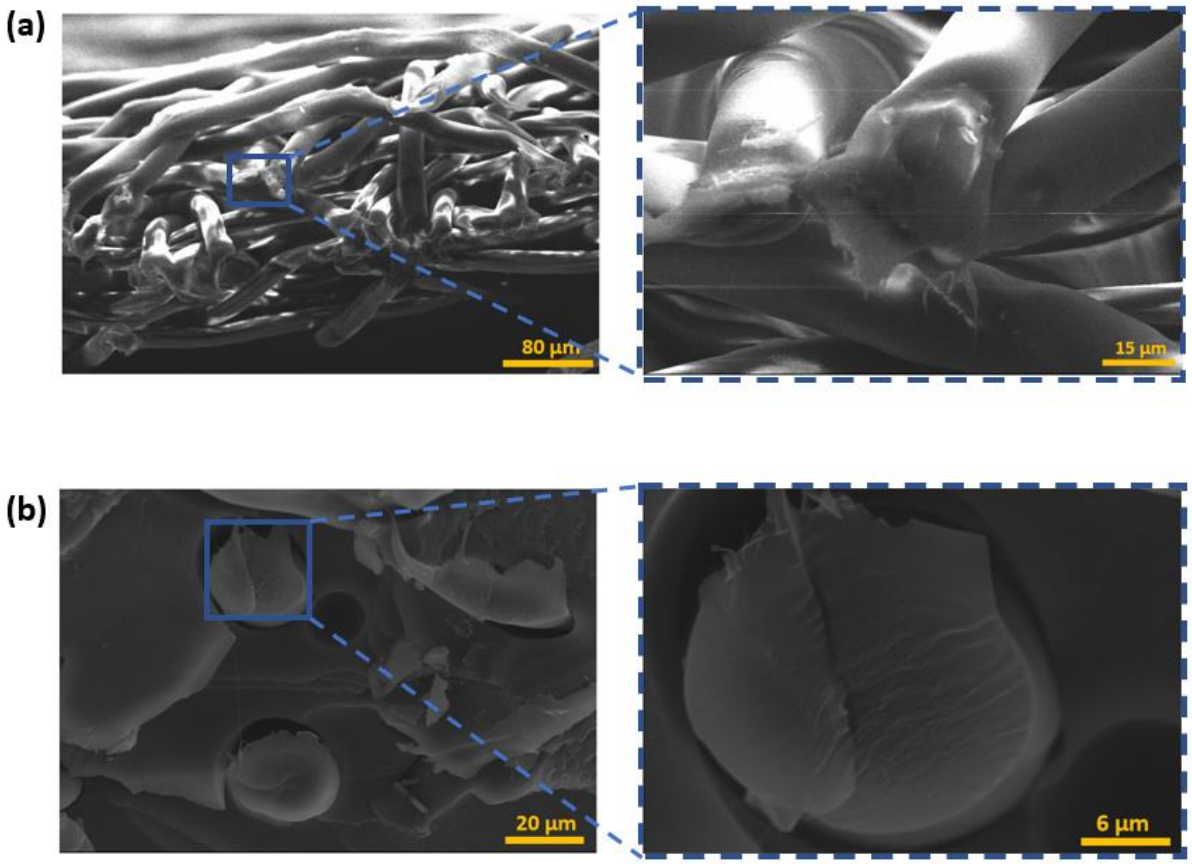

Figure 4.8. Cross-section SEM image of Cu_2O-coated PP fabric (a) after immersed in liquid nitrogen, and (b) after encapsulated with epoxy.

To get an accurate fit to the VI model, the measurement must be done until at least two oscillation amplitudes are observed in the reflectance. The setup explained in Section 3.2.6 collects a whole reflectance spectrum, but reflectance data at only one wavelength is needed for the VI method. In this work, the VI method is modified to observe reflectance as a function of deposition cycles (rather than time) since the purpose is to determine the Growth Per Cycle (GPC) of the coatings. For the Cu_2O coatings, reflectance was collected at a wavelength of 550 nm, with one reflectance measurement take after every 2 and 10 AP-SALD oscillations for glass and fabric substrates, respectively. For comparison, the measurements were done on borosilicate glass and spun-bond PP fabric substrates at 120 °C, both at a substrate oscillation speed of 1.5 cm/sec. The measured

reflectance data was fitted to the VI model by MATLAB's built-in function "lsqcurvefit", which is a nonlinear-least squares fitting method.

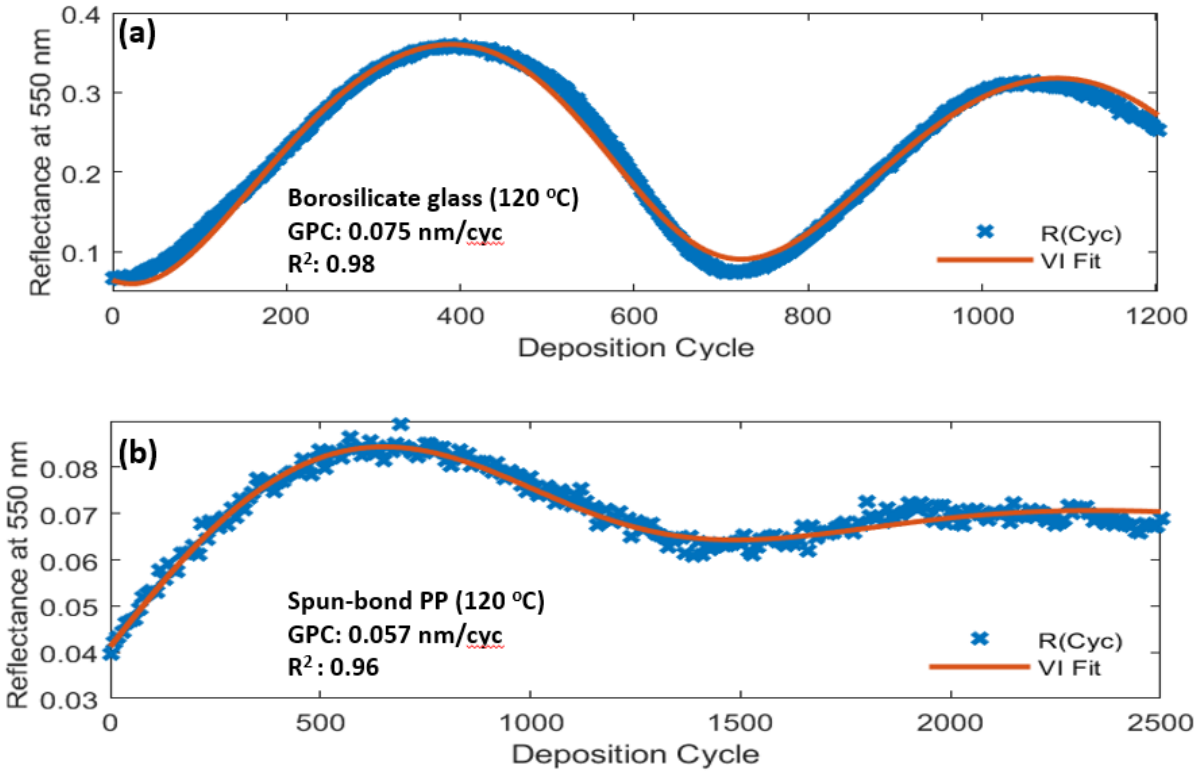

Figure 4.9. Collected reflectance intensity (blue crosses) at λ=550 nm as a function of deposition cycles for Cu_2O films coated on (a) borosilicate glass and (b) spun-bond PP fabric at 120 °C. The VI model fits to the data are shown in red.

Figure 4.9 shows the measured reflectance values as a function of the number of cycles for the Cu_2O deposited on (a) borosilicate glass and (b) PP fabric, as well as the VI model fits (red curves). The R^2 values were calculated for each plot, which shows how good the measurement fits the model. The fits to the VI model indicate GPCs of approximately 0.075 nm/ALD cycle and 0.057 nm/ALD cycle for the Cu_2O grown on borosilicate glass and PP fabrics, respectively. This value is three times higher than the growth rate reported before for Cu_2O deposition on glass by AP-SALD, which is on the order of 0.025 nm/cyc [48]. The higher value in this work could originate from the inclusion of SCVD (as a result of an unintentional wider gap between the reactor head and the substrate), which

increases the growth rate. Based on the estimated growth rate value, the thickness of coating in Figure 4.7 would be ~50-60 nm. These data show that the Cu_2O indeed has a low growth rate. It is interesting that the growth rates are close for glass and fabric substrates although the fabric surface does not have functional groups to bind the precursor, unlike glass, which has hydroxyl groups that can easily bind to the precursor. However, the fibrous morphology of the PP fabric may trap the precursors, increasing their deposition.

4.1.4. Robustness

For face mask applications, the robustness of the coatings is extremely important. Five different tests have been applied to the coated fabrics to test their robustness: washing, abrasion, tape adhesion, twisting and bending tests. The washing test is particularly important for reusable textiles. The samples were analyzed under SEM after each test.

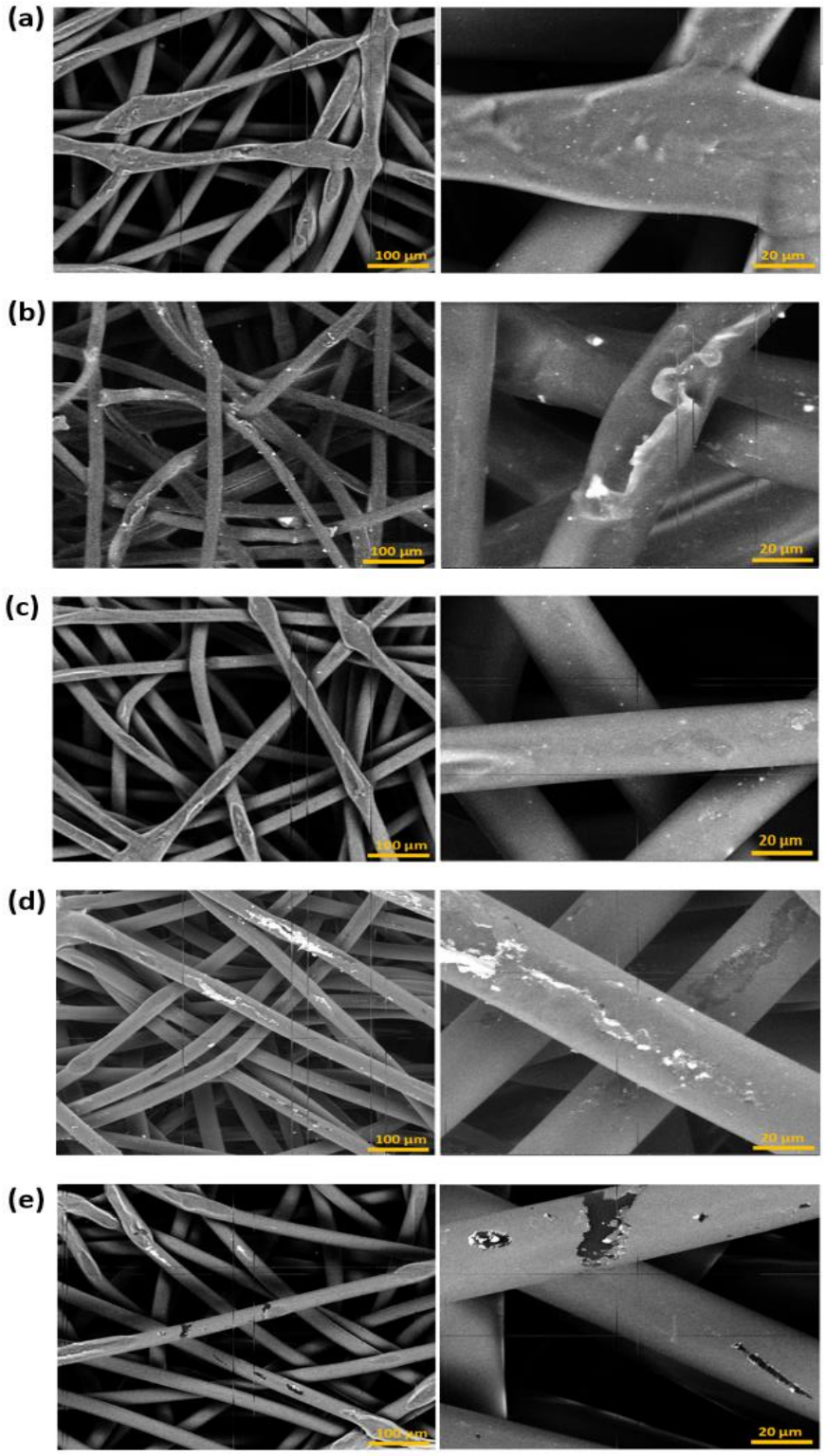

Figure 4.10. SEM images of Cu_2O – coated PP fabrics after (a) washing, (b) abrasion, (c) tape adhesion, (d) twisting and (e) bending tests.

Figure 4.10 shows the SEM images of coatings after applying the tests. Based on the SEM images, little damage was observed on any of the coatings. There are some white particles in Figure 4.10b from the abrasion test, which were verified by EDX to be aluminum pieces coming from the sandpaper. Only a few localized areas of damaged coating could be seen in the SEM images, several of which are shown in the right panel of Figure 4.10. This robustness could be associated with the fact that these coatings are very thin (on the nanometer scale). Another possible explanation is that the coatings form a continuous shell around the fibers, as can be seen in the SEM images, which it expected to increase the adhesion of the coatings.

4.2. ZnO – coated PP Fabrics

4.2.1. Optimization of Deposition Parameters

As explained in Chapter 2, deposition of ZnO has been achieved by many different techniques. It is also among the earliest compounds deposited by ALD, which was first reported in 1985 by using zinc acetate (ZnAc) and water as precursors [70]. Among many precursors available, diethyl zinc (DEZ) is the most common precursor for both conventional ALD and SALD due to its high vapor pressure, reactivity as well as large range of deposition temperature, starting from room temperature up to 350 °C [71, 72]. Yousfi et. al. proposes an ideal mechanism for ZnO deposition from DEZ and water precursors based on their quantitative measurements of atomic mass variations as follows [73]:

$$Zn(C_2H_5)_2\ (g)\ \rightarrow\ Zn(C_2H_5)_{ads} + C_2H_6\ (g) \tag{4.3}$$

$$Zn(C_2H_5)_{ads} + H_2O\ (g)\ \rightarrow\ Zn(OH)_{ads} + C_2H_6\ (g) \tag{4.4}$$

In this thesis, the PP fabrics have been coated with ZnO by AP-SALD at a deposition temperature of 100 °C since it is suitable for the PP. Unlike Cupraselect, it is possible to deposit thin films without

heating the DEZ bubbler, even at significantly lower flow rates compared to Cupraselect. The depositions were performed by setting the bubbler and carrier gas flow rates to 40 and 210 sccm for DEZ, and 100 and 200 sccm for water, respectively. The nitrogen flow was set to 1000 sccm, the gap between the reactor head and substrate was 100-150 μm, and the substrate oscillation speed was 1.5 cm/s.

4.2.2. Material Characterization

ZnO has a white color (transparent to visible light), which makes it hard to see the coatings visually as the PP fabric is also white. For that reason, the deposition was confirmed by SEM and EDX. The deposition was performed on a single layer of fabric and thus, the deposition was also observed on glass underneath the fabric. Figure 4.11a and b shows the SEM image of PP fabric coated with ZnO at 100 °C using 100 AP-SALD oscillations. An extremely smooth, conformal coating on the fibers is observed. The EDX data shown in Figure 4.11c indicates that there is zinc on the fabric, which provides strong evidence for the presence of ZnO.

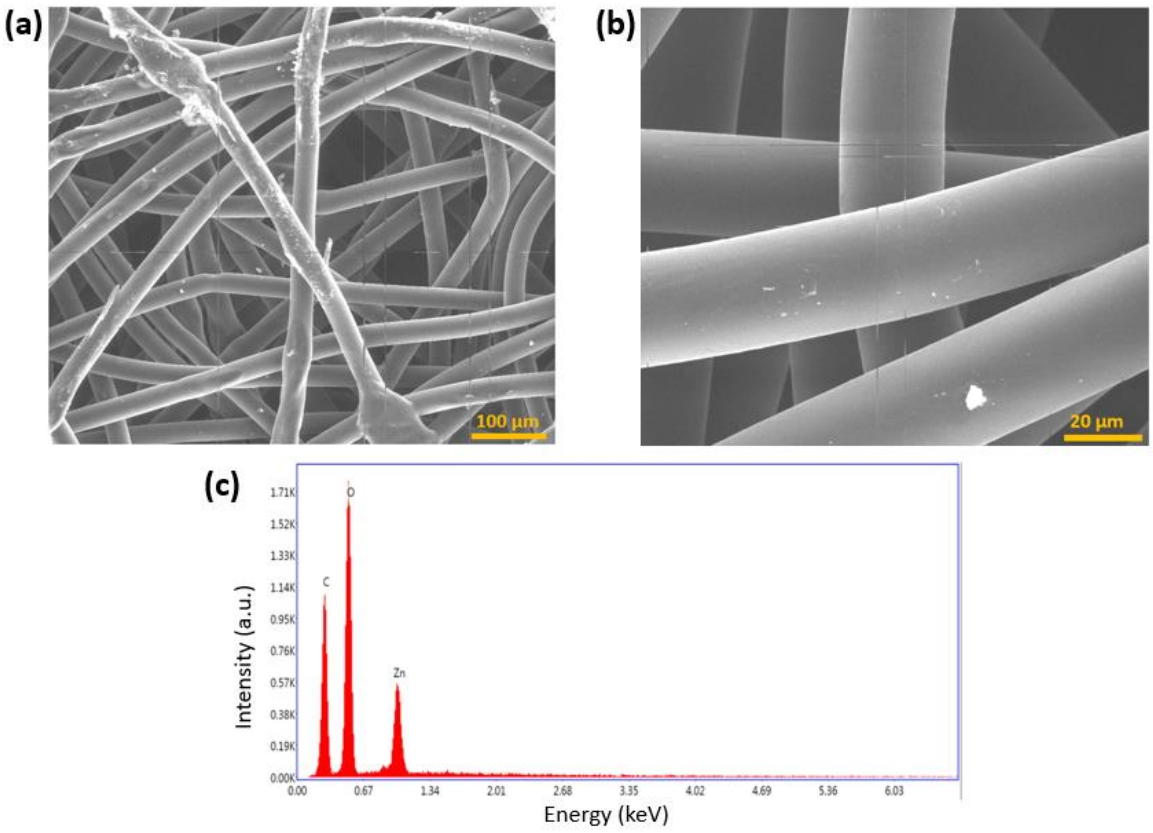

Figure 4.11. (a) and (b) SEM images of ZnO – coated PP fabric. (c) EDX spectrum of the coating.

In addition to the lab-scale AP-SALD that was used in this thesis, there is also a pilot-scale AP-SALD available in our lab. It allows the coating of areas up to 15 cm x 15 cm in size. To demonstrate the possibility for upscaling, coating of the PP fabric was also demonstrated with the pilot-scale SALD. A single layer of PP fabric sample (15 cm x 15 cm) was taped to a glass and oscillated at a speed of 8.0 cm/s at a deposition temperature of 75 °C for 650 AP-SALD oscillations. The precursor and carrier flow rates were set to 75 and 425 sccm for DEZ and 240 and 1360 sccm for water, respectively, and the nitrogen flow was set to 4800 sccm for the larger pilot-scale AP-SALD reactor head. The deposition was observed on the glass as well. Figure 4.12a and b shows the SEM images of the PP fabric coated with ZnO using the pilot-scale AP-SALD. Conformal coating of the PP fibers is again observed, but some cracks in the coatings were observed this time. It is likely that the coating deposited using the pilot-scale AP-SALD was thicker as more oscillations (650) were performed

compared to the previous lab-scale depositions (100), resulting in an accumulation of stress in the film and a greater likelihood of cracking due to applied strain (e.g., unintended flexing of the fabric). Figure 4.12c shows the EDX measurement of the coated fabric; the presence of zinc peaks again confirms the deposition of ZnO.

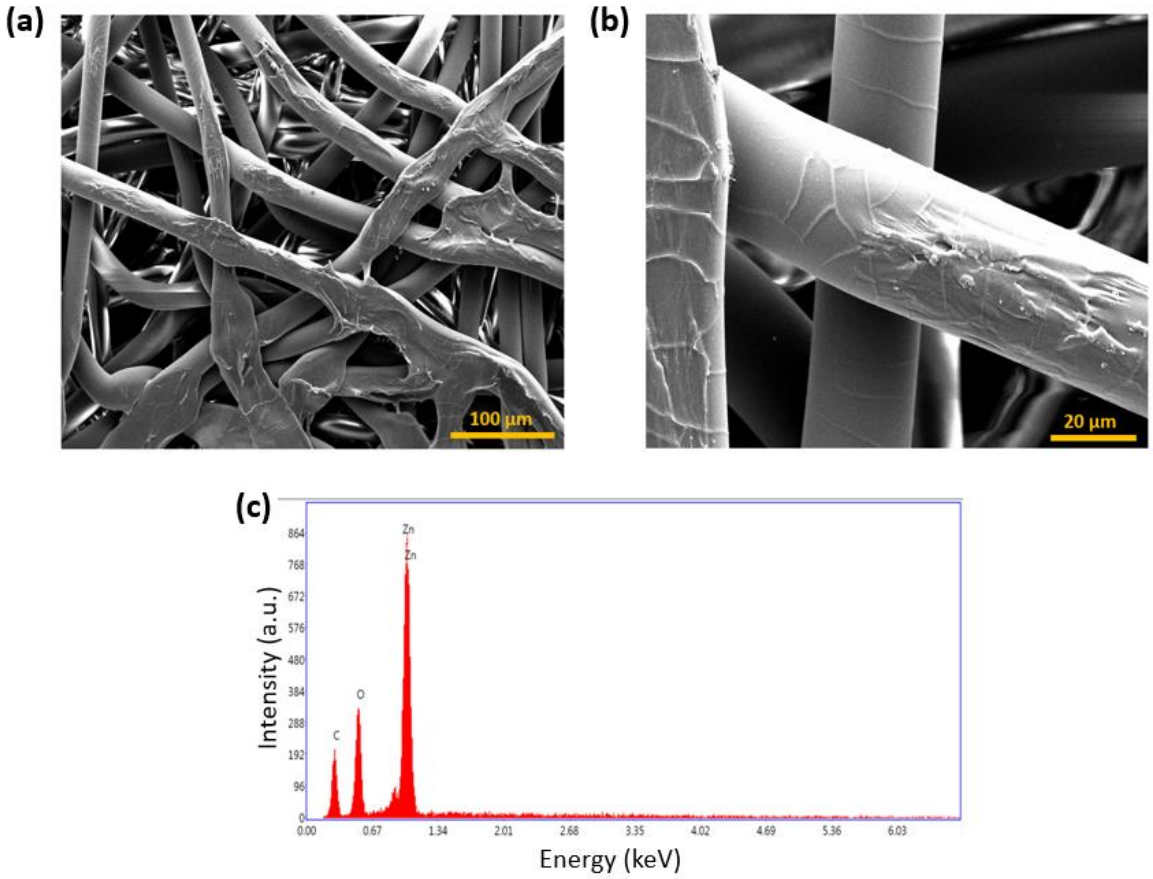

Figure 4.12. (a) and (b) SEM images of PP fabric coated with ZnO at 75 °C using a pilot-scale AP-SALD system and 650 cycles. (c) EDX spectrum of coatings.

In-situ reflectance measurements were again performed to identify the ZnO growth rate on the fabrics and glass samples. The lab-scale AP-SALD system was again used and for both cases, the oscillation speed was 1.5 cm/sec and the deposition temperature was 100 °C. Reflectance data at a single wavelength of 400 nm as a function of deposition cycles are shown in Figure 4.13 for the depositions on (a) glass and (b) PP fabric. The oscillatory patterns were clearly observed and could

be fitted to the VI model (red line) after the measurement to determine the GPC. The ZnO deposited on borosilicate glass and spun-bond PP at 100 °C has GPC values of 0.389 nm/ALD cycle and 0.22 nm/ALD cycle, respectively. The growth rate of ZnO by AP-SALD at 100 °C was reported as 0.255 nm/ALD cycle in the literature, which is close to the estimated value in this work [47]. Based on the estimated GPC, the thickness of ZnO coating on the PP fabric shown in Figure 4.11 was calculated as ~44 nm. Notably, the ZnO growth rate is very different on the glass and PP fabric. This is likely due to the different morphologies of the two substrates, which would result in different precursor flow patterns, and clearly demonstrates that it is not accurate to estimate the thickness of a coating on fabric, based on a growth rate measured on some other substrates. Hence, the in-situ reflectance method demonstrated here, is very valuable for accurately characterizing coating thicknesses on fabrics.

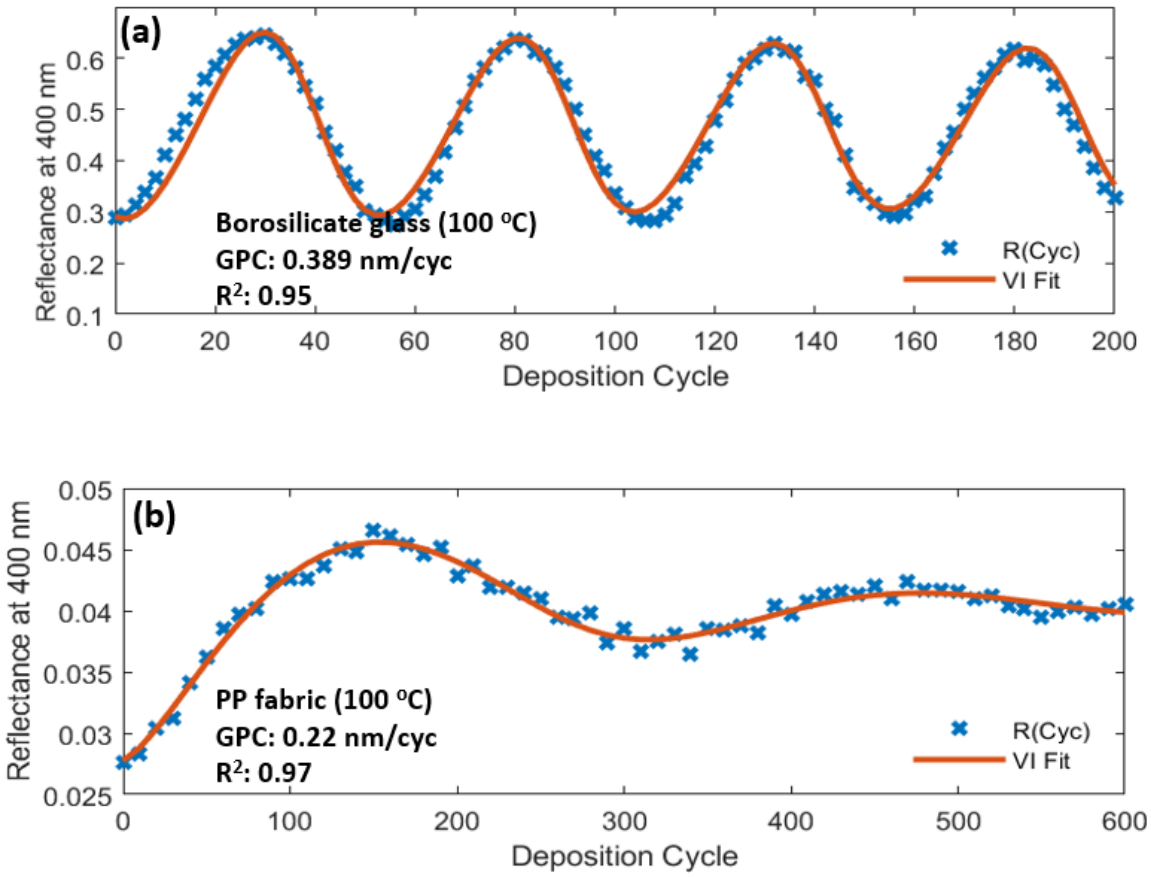

Figure 4.13. Collected reflectance intensity (blue crosses) at λ=400 nm as a function of deposition cycles for ZnO films coated on (a) borosilicate glass and (b) spun-bond PP fabric at 100 °C. The plot was fitted to VI model (red).

4.2.3. Robustness

ZnO-coated fabrics may be employed for their antibacterial [74] and UV protection properties [75]. For these applications, frequent washing of the fabrics is expected. Besides, other external forces can be applied, as mentioned before, which could damage the coatings. ZnO-coated PP fabrics were prepared by using the parameters given in Section 4.2.1. The depositions were performed at 100 °C with 100 AP-SALD oscillations. The estimated thickness of coatings is ~44 nm based on the VI model. Figure 4.14 shows the SEM images of ZnO-coated PP fabrics after five tests have been

applied: washing, abrasion, tape adhesion, twisting, and bending. Minimal damage to the coatings can be seen after the tests have been applied. Based on these tests, ZnO coatings also seem to be robust on the PP fabric.

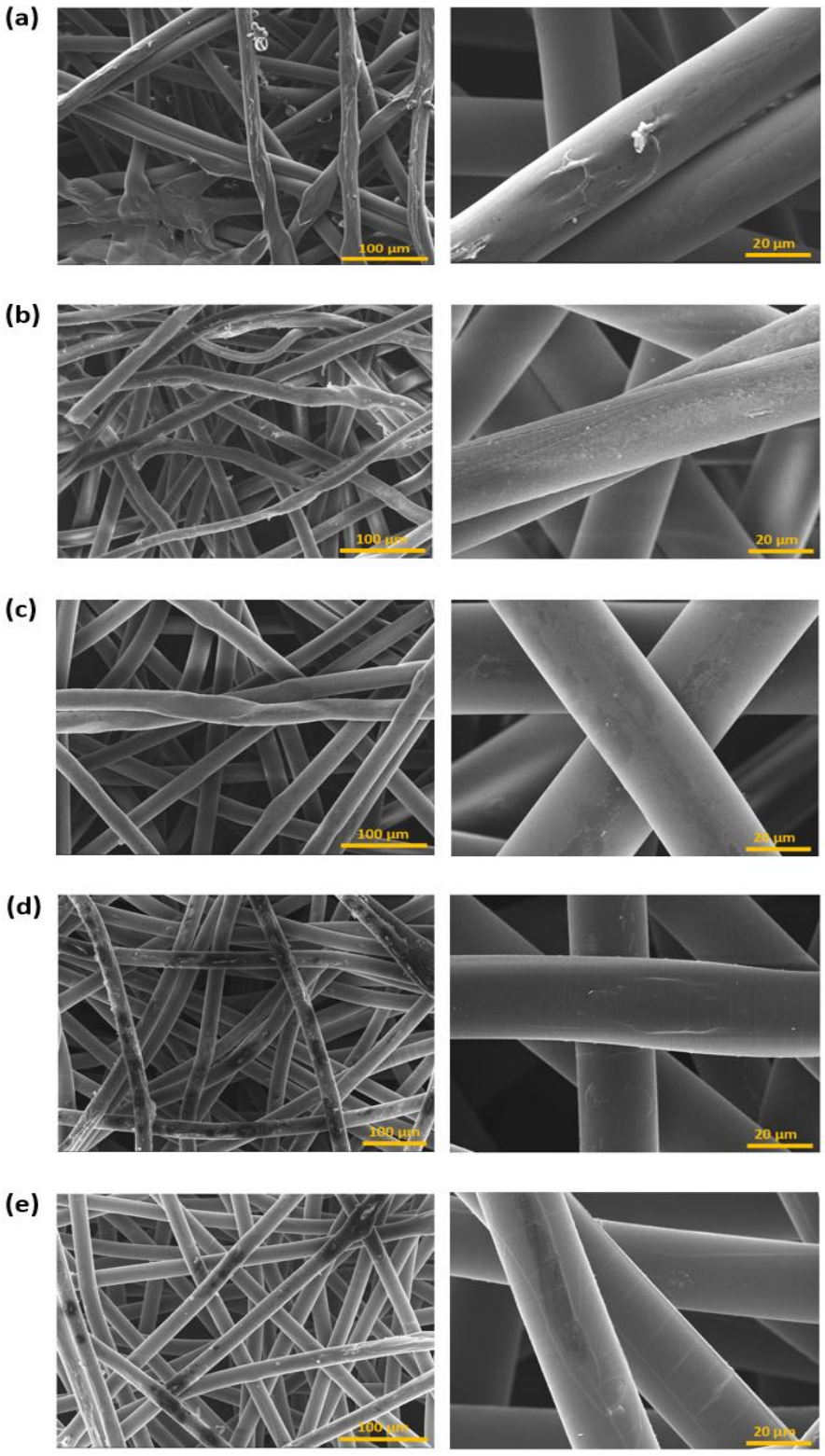

Figure 4.14. SEM images of ZnO – coated PP fabrics after (a) washing, (b) abrasion, (c) tape adhesion, (d) twisting and (e) bending tests.

Chapter 5

Other Tests

5.1. Filter Tests

5.1.1. Explanation of the Test and Its Importance

N95 respirators are a key piece of personal protective equipment against viral particles. Their N95 designation means that they have demonstrated the ability to filter at least 95% of NaCl particles with a median diameter of 0.075 μm [76]. The layers of face masks can be made of various materials, such as cotton, polyester, nylon and polypropylene [77]. Since PP is used in this work, this discussion will focus on mask layers made of PP. Nonwoven PP is typically used in PP-based masks because the fibers are arranged randomly in this system, which causes efficient filtration. Nonwoven PP can be processed in two main ways, which are spun-bonding (SB) and melt-blowing (MB). SB fibers are generally used for the outer and inner layers of respirators due to their larger diameters compared to MB fibers, which makes them suitable for mechanical support [78]. MB fibers can be used to make a middle mask layer. The middle layer plays the main filtering role due to the high packing density of the PP fibers as well as an electrostatic field applied during the manufacturing to enhance the filtration efficiency (Figure 5.1). The outer layer is the main part that is contacted most frequently, such as when putting the mask on and taking it off, handling it, and even unintentional contact when it is on your mouth. By coating the outer layer, contact-derived infections could be prevented.

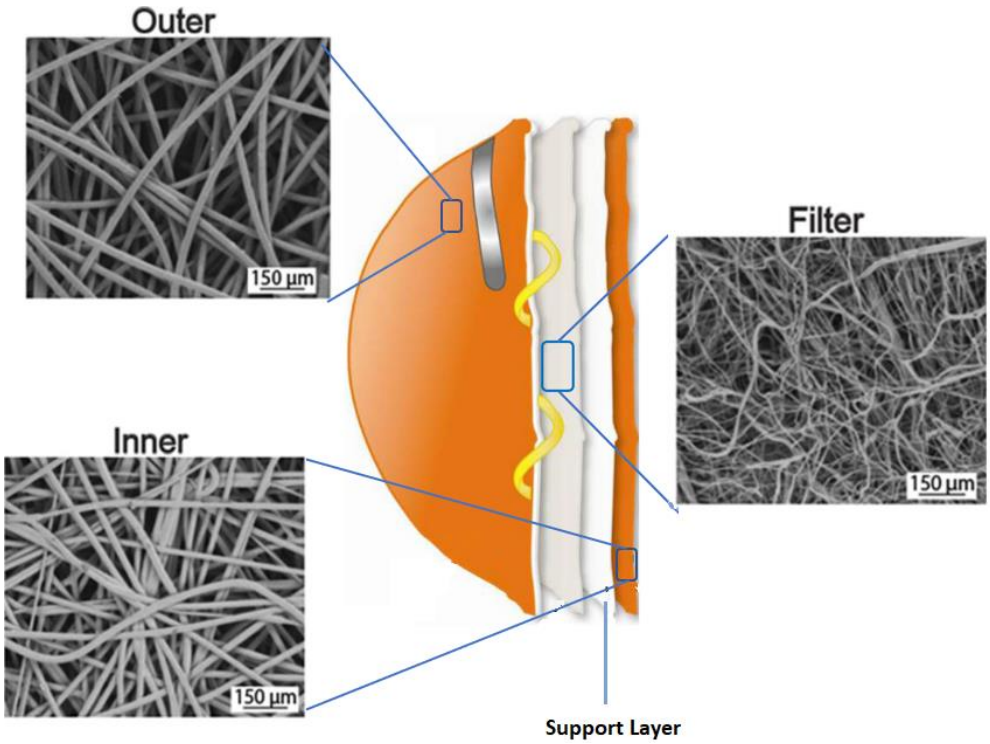

Figure 5.1. SEM images of inner, filter (middle), and outer layer of N95 respirators. Reprinted with permission from ref. 78. Copyright 2010 American Chemical Society

Filter tests were performed to ensure that the coatings developed in this work do not impact the filtering properties of the fabric layers. Filter tests were performed with the help of James Cheon (MASc student in Prof. Michael Tam's group) using an Automated Filter Tester (CERTITEST , Model 8130A, TSI, Inc.). A schematic diagram of the equipment is shown in Figure 5.2. The two most common aerosol particles used are NaCl and oil depending on the filter being tested. To do the measurement, the test filter is placed on the lower part of the filter holder. When the test is initiated, the pneumatic cylinder lowers the top part of the filter holder. Generated aerosols are neutralized and flow through the filter at a certain constant rate. Although using neutralized aerosols in the test defies the fact that one main way of adherence of aerosols to the fibers is through electrostatic interaction, this is how the National Institute for Occupational Safety and Health (NIOSH) tests the filters. The reason for using neutralized particles is that NIOSH considers the worst-case scenario, the filtration without any electrostatic interaction between filter and

aerosol. Thus, filtration efficiency determined with NIOSH standards may be lower than other standards, which use un-neutralized particles [79]. There are two light-scattering laser photometers, one below the filter, the other one is above the filter. The photometers measure the upstream and downstream aerosol concentrations at the same time. Penetration percentage (100 – filtration efficiency) can be calculated by taking the ratio of upstream and downstream concentrations.

One experimental challenge was that the original sample holder of the equipment has a diameter of 14 cm, which means the filter must be at least 14 cm x 14 cm in order to be able to run the experiment. However, the lab-scale AP-SALD is only capable of coating samples up to 5 cm x 7 cm. Taking this into account, a custom sample holder was made from acrylic with an area of 5 cm x 5 cm for the filter.

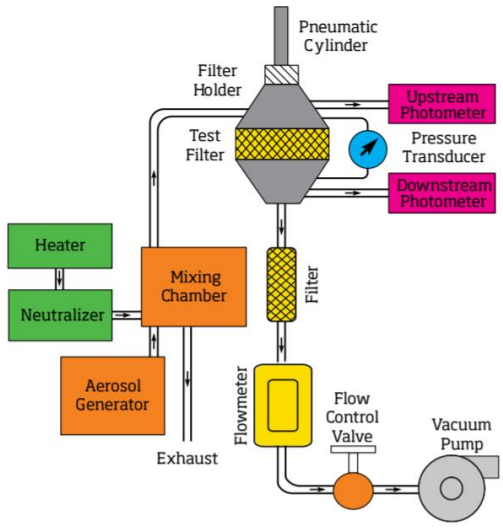

Figure 5.2. Schematic illustration of filter tester used (CERTITEST , Model 8130A, TSI, Inc.)

5.1.2. Filtration Efficiency of the Coated Fabrics

To do the measurement, the filter was sandwiched between two acrylic plates. NIOSH uses the flow rate of 85 L/min to represent inhalation of a worker at high workload [79]. This flow rate corresponds to a face velocity of 10.6 cm/s for a typical N95 respirator with a surface area 135 cm^2. Since the surface area exposed to the flow is smaller in this work, the flow rate was adjusted accordingly to keep the face velocity similar. Otherwise, face velocities, which are different from breathing conditions may skew the results. For that reason, the flow rate was set to 16.5 L/min to have a face velocity of ~11 cm/s. Generated aerosol particles had a size distribution with a count median diameter of 0.075 ± 0.020 μm. This size is smaller than the aerosols that carry viruses (0.25 – 4 μm), but NIOSH considers the worst-case scenario for filter tests [80].

As mentioned earlier in the chapter, the outer layer is not the main filter layer in a N95 respirator, and thus, it is not expected to have significant filtering capabilities. Figure 5.3 shows the measured penetration percentage for the various fabrics studied in this work. The outer spun-bond PP layer without any coating gives a penetration percentage of 92%. In other words, its filtration efficiency is only 8%. The purpose of this test is to make sure the coatings do not affect the filtering efficiency of the fabric even though it is not the main filter material. As mentioned earlier, Cu_2O depositions were performed on two layers of fabric (8 cm x 7 cm) taped to the stage by placing glass (7cm x 7cm) underneath and thus, penetration data for both layers are shown in Figure 5.3. Penetration percentages for all the samples are in the 90-96% range, and are the same as the uncoated sample, within experimental uncertainty. Nonetheless, a few observations are worth mentioning. First, a majority of the coated fabrics have a slightly higher penetration than the uncoated one, which defies the intuition that coating the fibers would decrease the size of the pores. A possible explanation is that the oxide coatings make the fibers smoother, which facilitates air flow through the pores. Another point is that the penetration appears to decrease with the number of deposition

cycles, which is expected due to the larger diameter of fibers with thicker coatings. Finally, a higher penetration is observed for the bottom layers in the Cu_2O – coated samples. It is possible that because the bottom layer is closer to the heating stage during the coating process, it receives more heat, and the morphology of its fibers are modified. While further investigation would be required to clarify some of these observations, these points are not critical. The important point is that this data demonstrates that coating the outer-layer PP fabric of a N95 respirator using AP-SALD does not affect the filtration efficiency of the fabric.

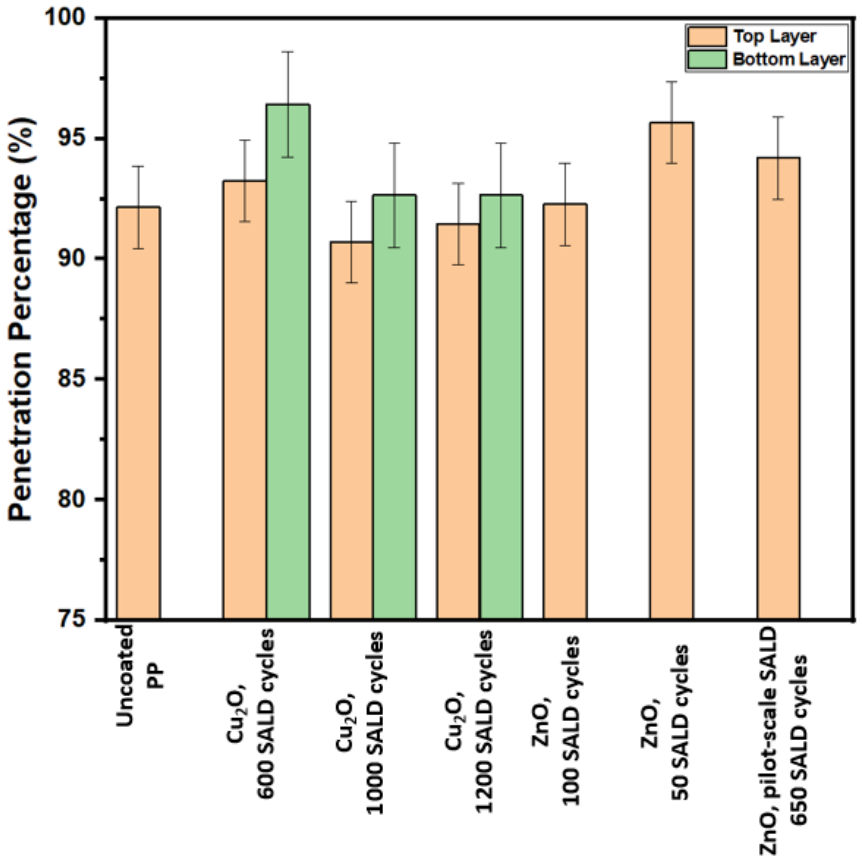

Figure 5.3. Penetration percentage of uncoated and coated fabrics. A count median diameter of aerosol particle size distribution is 0.075 ± 0.020 μm.

5.2. Cell Viability Test

5.2.1. Description of the Procedure

Since this work, especially Cu_2O – coated fabrics are aimed to be used in N95 respirators, cell viability tests are crucial to ensure the coatings do not adversely affect living cells, since skin contact and inhalation could occur. In this test, simple, directly applied, and noninvasive cell viability assays are used, which are the combination of two fluorescent dyes, Alamar blue (AB) and 5-carboxyfluorescein diacetate (CFDA). AB takes the role of measuring cellular metabolic activity, whereas CFDA is used to show cell membrane integrity [81].

This test was done by MSc student Samantha Lum in the lab of Dr. Stephanie DeWitte-Orr at Wilfrid Laurier University. To do this test, the coatings were first exposed to virus-free media. Next, after collecting the media, serial dilutions were done and added to Hep G2 cells. To measure the cell viability, cells were incubated with the AB and CFDA assays for 1 hr at 37 °C followed by the fluorescence measurement whose intensity is directly proportional with the number of living cells. For example, AB contains resazurin, which has a blue color and is non-fluorescent. Living cells reduce resazurin to red-colored, highly fluorescent resorufin. AB is very stable and nontoxic, which allows it to monitor cells for a long period of time. This is one main reason of using AB assay in many reports instead of other assays, such as [3-(4,5- dimethylthiazol-2-yl)-2,5-diphenyltetrazolium bromide] (MTT). Fluorescence measurements were done with a Synergy HT plate reader (BioTekWinooski, VT) at the excitation/emission wavelengths of 530/590 nm and 485/528 nm for AB and CFDA, respectively.

5.2.2. Effect of Cu_2O-coatings on Living Cells.

In this test, Cu_2O coatings deposited on both glass and PP fabric at 100 °C and 120 °C were tested along with other Cu, Cu_2O and CuO samples made by Abderrahime Sekkat from Dr. Muňoz – Rojas's

group (at the University of Grenoble-Alpes) for comparison. The details of the different samples tested are summarized in Table 5.1.

Table 5.1. Samples tested for cell viability test

Substrate	Coating	Deposition Temperature (°C)	AP-SALD system used (in our lab (UW) vs Grenoble)	Thickness (nm)
Glass	Cu_2O	120	UW	~20
Glass	Cu	120	Grenoble	20-30
Glass	Cu_2O	260	Grenoble	20-30
Glass	CuO	260	Grenoble	20-30
PP	Cu_2O	100	UW	Thickness 1 (thinner) Thickness 2 Thickness 3 (thicker)
PP	Cu_2O	120	UW	Thickness 1 (thinner) Thickness 2 Thickness 3 (thicker)
PP	CuO	120	Grenoble	-

Figure 5.4 shows the viability test results for the coatings on glass. Rather than showing the control sample (plain glass and PP fabric heated at corresponding temperatures) in the plot, it is reflected directly on the y-axis by converting the y-axis to percentage of the fluorescence intensity readings in the control sample. This means that any value below 100% could be an indicator of toxicity because there would be a smaller number of living cells than the control sample, meaning some cells are killed. In the AB measurements, the Cu_2O sample deposited at 260 °C shows a lower percentage value, which could be the indication of potential toxicity of that sample. In the CFDA assay, all the values for all samples are lower compared to those in AB, but CuO and Cu_2O at 260 °C show even lower values. Based on this data, it seems that the coatings produced at the higher deposition temperature of 260 °C show more toxicity against the living cells.

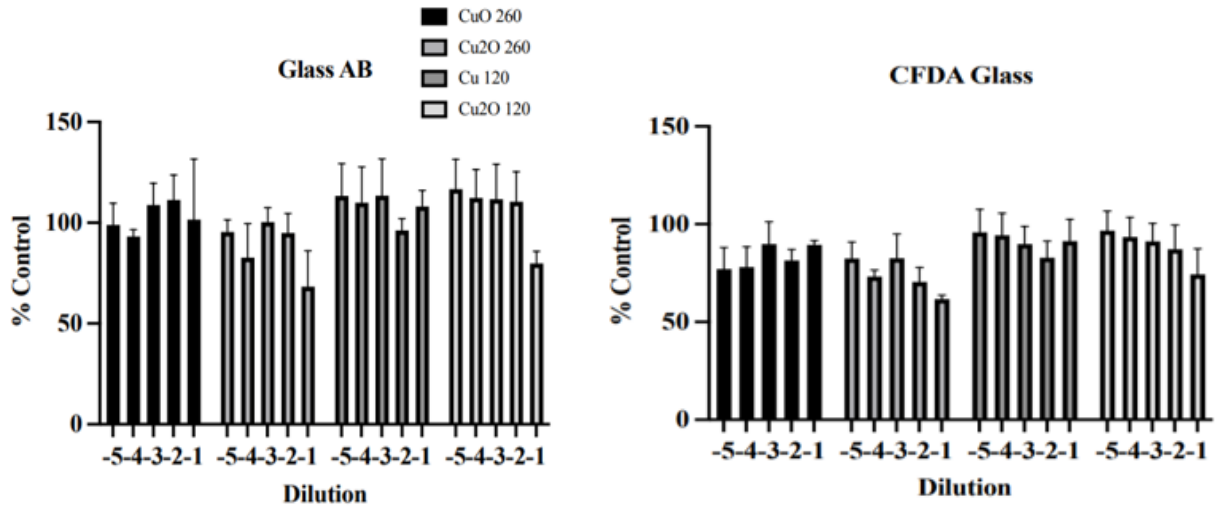

Figure 5.4. Cell viability of glass samples in AB and CFDA assays. Vertical axis shows the percentage of living cells relative to those in control sample whereas in horizontal axis, each sample undergoes 5 series of dilutions.

Two deposition temperatures, 100 °C and 120 °C, were tested for Cu_2O – coated fabric samples. For each temperature, three different thicknesses were chosen based on the color intensity of the coatings, as the exact thicknesses could not be measured at that time. In addition, CuO deposited at 120 °C on PP fabric was also tested for comparison. Again, the measurements with CFDA indicate a lower number of cells compared to those with AB. Overall, the fabric coated with Cu_2O at 100 °C did not show any toxicity, regardless of the coating thickness, whereas the coatings deposited at 120 °C could have some toxicity against living cells. This in contrast to the glass samples deposited at 120 °C that did not show any toxicity in Figure 5.4. This difference could be related to different leaching rates of coatings on different substrates. Nonetheless, these results indicate that the PP fabrics coated with Cu_2O at 100 °C do not appear to be cytotoxic and hence could be safe for use in N95 respirators.

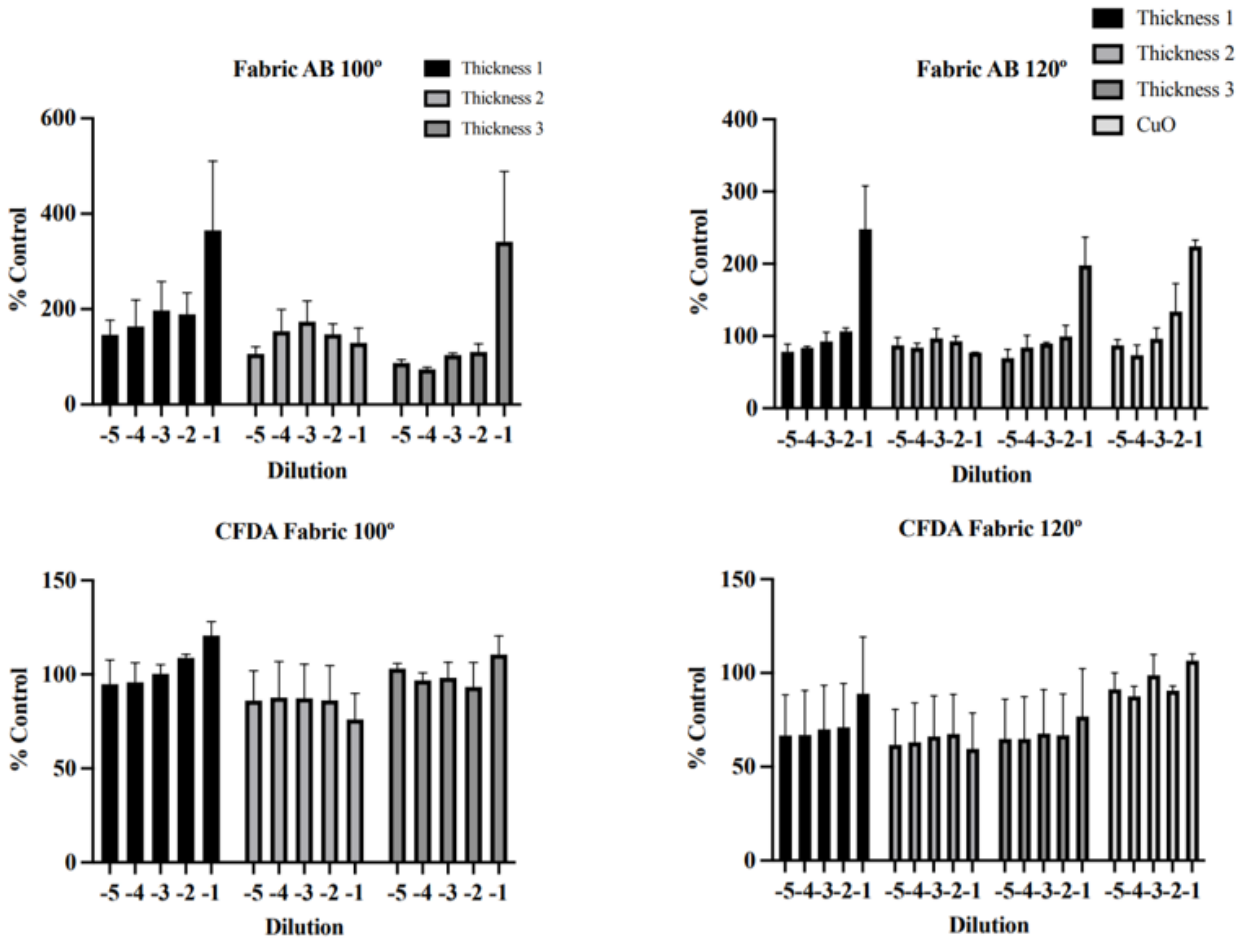

Figure 5.5. Cell viability of fabric samples in AB and CFDA assays.

Chapter 6

Conclusion and Future Work

In this thesis, it has been demonstrated, by coating spun-bond PP with Cu_2O and ZnO, that textiles can be conformally coated by lab-scale as well as pilot-scale AP-SALD. A PP fabric was coated with CuO_x by using Cupraselect as a precursor at a temperature of 100-120 °C, which is a suitable temperature for PP fabrics. The deposited CuO_x coatings were confirmed to be predominantly Cu_2O by XRD, UV-vis spectroscopy, and XPS.

When modifications are made to the fabrics, the first thing to study is the robustness of the modified fabric as fabrics are generally subjected to washing and other kind of mechanical forces. The robustness of coatings was tested with five different mechanical tests: washing, abrasion, tape adhesion, twisting and bending. No significant damage to the coatings was observed after any of these tests were applied. Thickness measurement is another challenge with fabric coatings. After failing with other approaches, the growth rate of fabric coatings was estimated from in-situ reflectometry by applying a VI model. The GPC of Cu_2O coated on PP fabric at 120 °C was estimated as 0.057 nm/ALD cycle whereas it was 0.1856 nm/ALD cycle for ZnO – coated PP fabrics at 100 °C.

Since the substrate is a spun-bond PP, which is used as an outer layer of N95 respirators, filter tests were performed to make sure the filtration efficiency is not affected by the coatings, although it is unlikely due to the large pores of spun-bond PP. The uncoated fabric had a 92% +/- 2% penetration (filtration efficiency of 8%) and the penetration percentage of coated fabrics was in the range of 90% to 96% indicating that the coatings do not impact the filtration efficiency.

Finally, the aimed application, especially for Cu_2O – coated fabrics, is antiviral N95 respirators. For that reason, cell viability tests were performed on Cu – based coatings. It seems that increasing the deposition temperature also increases the likelihood of the coatings being toxic to living cells. The deposition temperature of 100 °C was the most ideal among the tested samples in terms of cell viability performance.

Study of the antiviral performance of the coated fabrics is required next. It is worth noting that fabrics are generally exposed to air and moisture, especially in face mask applications since a person is continuously breathing. As a result, Cu_2O coatings on fabrics could oxidize to CuO in long term, which would modify the physical, optical, as well as antiviral properties. Deeper work should be conducted on effect of air and moisture on Cu_2O coatings. Besides, there is still more room to improve this work. For example, Cu_2O was deposited using Cupraselect as the precursor, which is quite expensive. Other cheaper alternatives should be investigated. Due to the porosity of the fabric, the majority of the precursor gases pass through the fabric, which causes inefficiency in precursor usage. Better approaches, such as coating multiple layers at once, need to be designed to avoid precursor waste. Furthermore, the accuracy of the thicknesses measured by the VI model should be confirmed with other possible techniques, e.g. transmission electron microscopy. Finally, the yellow appearance of the Cu_2O may not be appropriate for some applications. Therefore, the deposition of transparent Cu_2O coatings could be investigated.

Bibliography

[1] Worldometer Real Time World Statistics. https://www.worldometers.info/

[2] Ozili, P. K. and Arun, T., Spillover of COVID-19: Impact on the Global Economy (March 27, 2020). http://dx.doi.org/10.2139/ssrn.3562570

[3] Kawohl W., Nordt C. COVID-19, unemployment, and suicide. *Lancet Psychiatry.* 2020;7(May (5)):389–390. https://doi.org/10.1016/S2215-0366(20)30141-3

[4] Aboubakr, HA, Sharafeldin, TA, Goyal, SM. Stability of SARS-CoV-2 and other coronaviruses in the environment and on common touch surfaces and the influence of climatic conditions: A review. *Transbound Emerg Dis*. 2021; 68: 296– 312. https://doi.org/10.1111/tbed.13707

[5] Stelzer-Braid, S., Oliver, B. G., Blazey, A. J., Argent, E., Newsome, T. P., Rawlinson, W. D., & Tovey, E. R. (2009). Exhalation of respiratory viruses by breathing, coughing, and talking. *Journal of Medical Virology*, **81**(9), 1674–1679. https://doi.org/10.1002/jmv.21556

[6] Prather KA, Wang CC, Schooley RT: Reducing transmission of SARS-CoV-2. *Science* 2020, 368:1422-1424. https://www.science.org/doi/10.1126/science.abc6197

[7] Chughtai, A.A., Stelzer-Braid, S., Rawlinson, W. *et al.* Contamination by respiratory viruses on outer surface of medical masks used by hospital healthcare workers. *BMC Infect Dis* **19,** 491 (2019). https://doi.org/10.1186/s12879-019-4109-x

[8] Muhammad, W., Zhai, Z., Gao*, C., Antiviral Activity of Nanomaterials against Coronaviruses. *Macromol. Biosci*. 2020, 20, 2000196. https://doi.org/10.1002/mabi.202000196

[9] Carvalho, A. P. A., Conte-Junior, C. A., Recent Advances on Nanomaterials to COVID-19 Management: A Systematic Review on Antiviral/Virucidal Agents and Mechanisms of SARS-CoV-2 Inhibition/Inactivation. *Global Challenges* 2021, 5, 2000115. https://doi.org/10.1002/gch2.202000115

[10] Behzadinasab, S., Chin, A., Hosseini, M., Poon, L., and Ducker, W., A. A Surface Coating that Rapidly Inactivates SARS-CoV-2 *ACS Applied Materials & Interfaces* **2020** *12* (31), 34723-34727. https://doi.org/10.1021/acsami.0c11425

[11] Hosseini, M., Chin, A., W., H., Behzadinasab, S., Leo L. M. Poon L., and Ducker, W., A., Cupric Oxide Coating That Rapidly Reduces Infection by SARS-CoV-2 via Solids, *ACS Applied Materials & Interfaces* **2021** *13* (5), 5919-5928. https://doi.org/10.1021/acsami.0c19465

[12] Ermini, M., L., and Voliani, V., Antimicrobial Nano-Agents: The Copper Age, *ACS Nano* **2021** *15* (4), 6008-6029. https://doi.org/10.1021/acsnano.0c10756

[13] Delumeau L-V, Asgarimoghaddam H., Alkie T., Jones A. J. B., Lum S., Mistry K., Aucoin M. G., DeWitte-Orr S., and Musselman K. P., "Effectiveness of antiviral metal and metal oxide thin-film coatings against human coronavirus 229E", *APL Materials* 9, 111114 (2021) https://doi.org/10.1063/5.0056138

[14] Verbič A, Gorjanc M, Simončič B. Zinc Oxide for Functional Textile Coatings: Recent Advances. *Coatings*. 2019; 9(9):550. https://doi.org/10.3390/coatings9090550

[15] https://www.epa.gov/newsreleases/epa-registers-copper-surfaces-residual-use-against-coronavirus

[16] Gattinoni, C.; Michaelides, A. Atomistic Details of Oxide Surfaces and Surface Oxidation: The Example of Copper and Its Oxides. *Surf. Sci. Rep.* **2015**, *70*, 424– 447. https://doi.org/10.1016/j.surfrep.2015.07.001

[17] Zoolfakar, A. S.; Rani, R. A.; Morfa, A. J.; O'Mullane, A. P.; Kalantar-zadeh, K. Nanostructured copper oxide semiconductors: A perspective on materials, synthesis methods and applications *J. Mater. Chem. C* **2014**, 2, 5247– 5270. https://doi.org/10.1039/C4TC00345D

[18] P. Poulopoulos, S. Baskoutas, S. D. Pappas, C. S. Garoufalis, S. A. Droulias, A. Zamani, and V. Kapaklis, "Intense Quantum Confinement Effects in Cu_2O Thin Films," *J. Phys. Chem. C* **115**(30), 14839–14843 (2011). https://doi.org/10.1021/jp203145n

[19] Meyer, B.K., Polity, A., Reppin, D., Becker, M., Hering, P., Klar, P.J., Sander, T., Reindl, C., Benz, J., Eickhoff, M., Heiliger, C., Heinemann, M., Bläsing, J., Krost, A., Shokovets, S., Müller, C. and Ronning, C. (2012), Binary copper oxide semiconductors: From materials towards devices. *Phys. Status Solidi B*, 249: 1487-1509. https://doi.org/10.1002/pssb.201248128

[20] Tortella, G., R., Pieretti, J., C., Rubilar, O., Fernández-Baldo, M., Benavides-Mendoza, A., Diezm M., C. & Seabra, A., B. (2021) Silver, copper and copper oxide nanoparticles in the fight against human viruses: progress and perspectives, *Critical Reviews in Biotechnology*, DOI: 10.1080/07388551.2021.1939260

[21] Sushma, Y., Jain A and Malhotra P. A review on the sustainable routes for the synthesis and applications of cuprous oxide nanoparticles and their nanocomposites. (2019), *Green Chem.* 21 937–55. https://doi.org/10.1039/C8GC03303J

[22] Hu, H., Kremenakova, D., Militký, J., Periyasamy, A., P., Textiles and Their Use In Microbial Protection, 2021 taylorfrancis.com https://doi.org/10.1201/9781003140436

[23] Imani, S.M.; Ladouceur, L.; Marshall, T.; Maclachlan, R.; Soleymani, L.; Didar, T.F. Antimicrobial Nanomaterials and Coatings: Current Mechanisms and Future Perspectives to Control the Spread of Viruses Including SARS-CoV-2. *ACS Nano* 2020, *14*, 12341–12369. https://doi.org/10.1021/acsnano.0c05937

[24] Ruiz-Hitzky, E., Darder, M., Wicklein, B., Ruiz-Garcia, C., Martín-Sampedro, R., del, G., Aranda, P., Nanotechnology Responses to COVID-19. *Adv. Healthcare Mater.* 2020, 9, 2000979. https://doi.org/10.1002/adhm.202000979

[25] Mallakpour, S., Azadi, E., and Hussain, C., M., The latest strategies in the fight against the COVID-19 pandemic: the role of metal and metal oxide nanoparticles, *New J. Chem.*, 2021, **45**, 6167–6179. https://doi.org/10.1039/D1NJ00047K

[26] Wang, N., Ferhan, A., R., Yoon, B., K., Jackman, J., A., Cho, N., J., and Majima, T., Chemical design principles of next-generation antiviral surface coatings, *Chem. Soc. Rev.,* 2021, 50, 9741-9765. https://doi.org/10.1039/D1CS00317H

[27] Kim I., Viswanathan, K., Kasi, G., Thanakkasaranee, S., Sadeghi, K., & Seo, J. (2020) ZnO Nanostructures in Active Antibacterial Food Packaging: Preparation Methods, Antimicrobial Mechanisms, Safety Issues, Future Prospects, and Challenges*, Food Reviews International*, DOI: 10.1080/87559129.2020.1737709

[28] Ü. Özgür, Ya. I. Alivov, C. Liu, A. Teke, M. A. Reshchikov, S. Doğan, V. Avrutin, S.-J. Cho, and H. Morkoç , "A comprehensive review of ZnO materials and devices*", Journal of Applied Physics* 98, 041301 (2005). https://doi.org/10.1063/1.1992666

[29] Ran J, He M, Li W, Cheng D, Wang X. Growing ZnO Nanoparticles on Polydopamine-Templated Cotton Fabrics for Durable Antimicrobial Activity and UV Protection. *Polymers*. 2018; 10(5):495. https://doi.org/10.3390/polym10050495

[30] Ramamurthy P, Chellamani KP, Dhurai B, ThankaRajan SP,Subramanian B, Santhini E. Antimicrobial Characteristics of Pulsed Laser Deposited Metal Oxides on Polypropylene

Hydroentangled Nonwovens for Medical Textiles. *FIBRES & TEXTILES in Eastern Europe* 2017; 25, 2(122): 112-119. DOI: 10.5604/12303666.1228192

[31] Kumar S., Karmacharya M., Joshi, S., R., Gulenko, O., Park, J., Kim G., H., and Cho Y., K., Photoactive Antiviral Face Mask with Self-Sterilization and Reusability, *Nano Letters* **2021** *21* (1), 337-343. https://doi.org/10.1021/acs.nanolett.0c03725

[32] Jung S, Yang J-Y, Byeon E-Y, Kim D-G, Lee D-G, Ryoo S, Lee S, Shin C-W, Jang HW, Kim HJ, Lee S. Copper-Coated Polypropylene Filter Face Mask with SARS-CoV-2 Antiviral Ability. *Polymers*. 2021; 13(9):1367. https://doi.org/10.3390/polym13091367

[33] M.-L. Huang, Z. Cai, Y.-Z. Wu, S.-G. Lu, B.-S. Luo, Y.-H. Li, Metallic coloration on polyester fabric with sputtered copper and copper oxides films, *Vacuum*, 178 (2020), p. 109489. https://doi.org/10.1016/j.vacuum.2020.109489

[34] X.H. Yuan, W.Z. Xu, F.L. Huang, D.S. Chen, Q.F. Wei, Polyester fabric coated with Ag/ZnO composite film by magnetron sputtering, *Appl. Surf. Sci*., 390 (2016), pp. 863-869. https://doi.org/10.1016/j.apsusc.2016.08.164

[35] Fernades, F, Filho, ER, Souza, I, et al. Novel synthesis of copper oxide on fabric samples by cathodic cage plasma deposition. Polym Adv Technol. 2020; 31: 520– 526. https://doi.org/10.1002/pat.4792

[36] Mantecca P., Kasemets K., Deokar A., Perelshtein I., Gedanken A., Bahk Y. K., Kianfar B., and Wang J., Airborne Nanoparticle Release and Toxicological Risk from Metal-Oxide-Coated Textiles: Toward a Multiscale Safe-by-Design Approach. *Environmental Science & Technology* **2017** *51* (16), 9305-9317. https://doi.org/10.1021/acs.est.7b02390

[37] Borkow, G. and Gabbay, J. (2004), Putting copper into action: copper-impregnated products with potent biocidal activities. The FASEB Journal, 18: 1728-1730. https://doi.org/10.1096/fj.04-2029fje

[38] R. Borda d' Água, R. Branquinho, M. P. Duarte, E. Maurício, A. L. Fernando, R. Martins and E. Fortunato, Efficient coverage of ZnO nanoparticles on cotton fibres for antibacterial finishing using a rapid and low cost *in situ* synthesis, *New J. Chem.*, 2018, **42**, 1052. https://doi.org/10.1039/C7NJ03418K

[39] T.I. Shaheen, M.E. El-Naggar, A.M. Abdelgawad, A. Hebeish, Durable antibacterial and UV protections of in situ synthesized zinc oxide nanoparticles onto cotton fabrics, *Int. J. Biol. Macromol*., 83 (2016), pp. 426-432. https://doi.org/10.1016/j.ijbiomac.2015.11.003

[40] Akyildiz H. I., Diler S., and Islam S., Evaluation of TiO2 and ZnO atomic layer deposition coated polyamide 66 fabrics for photocatalytic activity and antibacterial applications, *Journal of Vacuum Science & Technology A* 39, 022405 (2021). https://doi.org/10.1116/6.0000761

[41] Karttunen, A. J., Sarnes, L., Townsend, R., Mikkonen, J., Karppinen, M., Flexible Thermoelectric ZnO–Organic Superlattices on Cotton Textile Substrates by ALD/MLD, *Adv. Electron. Mater.* 2017, 3, 1600459. https://doi.org/10.1002/aelm.201600459

[42] Sun, L., Yuan, G., Gao, L. *et al.* Chemical vapour deposition. *Nat Rev Methods Primers* **1,** 5 (2021). https://doi.org/10.1038/s43586-020-00005-y

[43] R.L. Puurunen, Surface chemistry of atomic layer deposition: A case study for the trimethylaluminum/water process*, J. Appl. Phys*. 97 (2005) 121301. https://doi.org/10.1063/1.1940727

[44] Muñoz-Rojas, D., Nguyen, V., H., Masse de la Huerta, C., Aghazadehchors, S., Jiménez, C., and Bellet D., "Spatial Atomic Layer Deposition (SALD), an emerging tool for energy materials. Application to new-generation photovoltaic devices and transparent conductive materials," *Comptes Rendus Physique,* vol. 18, no. 7-8, pp. 391–400, 9 2017. https://doi.org/10.1016/j.crhy.2017.09.004

[45] Illiberi, A., Roozeboom, F., and Poodt, P., "Spatial Atomic Layer Deposition of Zinc Oxide Thin Films," *ACS Applied Materials & Interfaces*, vol. 4, no. 1, pp. 268–272, 1 2012. https://doi.org/10.1021/am2013097

[46] Levy, D., H., Nelson, S., F., and Freeman, D., "Oxide Electronics by Spatial Atomic Layer Deposition," *Journal of Display Technology*, vol. 5, no. 12, pp. 484–494, 12 2009. https://doi.org/10.1109/JDT.2009.2022770

[47] Mistry, K., Jones A., Kao, M., Yeow T. W. K., Yavuz M., and Musselman K. P., In-situ observation of nucleation and property evolution in films grown with an atmospheric pressure spatial atomic layer deposition system. *Nano Express* **1**, 010045 (2020). https://doi.org/10.1088/2632-959X/ab976c

[48] Muñoz-Rojas D., Jordan, M., Yeoh, C., Marin, A., T., Kursumovic, A., Dunlop, L., A., Iza, D., C., Chen, A., Wang, H., and MacManus Driscoll, J., L., "Growth of 5 cm 2 V 1 s 1 mobility, p-type Copper(I) oxide (Cu2O) films by fast atmospheric atomic layer deposition (AALD) at 225C and below," *AIP Advances,* vol. 2, no. 4, p. 042179, 12 2012. https://doi.org/10.1063/1.4771681

[49] Sekkat, A., Nguyen, V.H., Masse de La Huerta, C.A. *et al.* Open-air printing of Cu_2O thin films with high hole mobility for semitransparent solar harvesters. *Commun Mater* **2,** 78 (2021). https://doi.org/10.1038/s43246-021-00181-8

[50] R. L. Z. Hoye, B. Ehrler, M. L. Bohm, D. Munoz-Rojas, R. M. Altamimi, A. Y. Alyamani, Y. Vaynzof, A. Sadhanala, G. Ercolano, N. C. Greenham, R. H. Friend, J. L. MacManus-Driscoll, and K. P. Musselman, Research Update: Atmospheric pressure spatial atomic layer deposition of ZnO thin films: Reactors, doping, and devices, *Adv. Energy Mater*. 4, 1301544 (2014). https://doi.org/10.1063/1.4916525

[51] Illiberi, A., Scherpenborg, R., Wu, Y., Roozeboom, F., and Poodt, P., Spatial Atmospheric Atomic Layer Deposition of AlxZn1−xO, *ACS Applied Materials & Interfaces* 2013 *5* (24), 13124-13128. https://doi.org/10.1021/am404137e

[52] Nakano, Y., Saeki, S., and Morikawa, T. "Optical bandgap widening of *p*-type Cu2O films by nitrogen doping", *Appl. Phys. Lett*. 94, 022111 (2009). https://doi.org/10.1063/1.3072804

[53] Nolan, M., and Elliott, S., D., Tuning the Transparency of Cu2O with Substitutional Cation Doping, *Chemistry of Materials* 2008 *20* (17), 5522-5531. https://doi.org/10.1021/cm703395k

[54] Laidoudi, S., Bioud, A., Y.,Azizi, A., Schmerber, G., Bartringer, J., Barre, S. and Dinia, A., Growth and characterization of electrodeposited Cu2O thin films, 2013 *Semicond. Sci. Technol.* **28** 115005. https://doi.org/10.1088/0268-1242/28/11/115005

[55] Coulter, J.B. and Birnie, D.P., III (2018), Assessing Tauc Plot Slope Quantification: ZnO Thin Films as a Model System. *Phys. Status Solidi B*, 255: 1700393. https://doi.org/10.1002/pssb.201700393

[56] Zadora, G. and Michalska, A. (2021). Scanning Electron Microscopy. In Analytical Techniques in Forensic Science (eds R. Wolstenholme, S. Jickells and S. Forbes). https://doi.org/10.1002/9781119373421.ch9

[57] Lee HL., Flynn N.T. (2006) X-RAY PHOTOELECTRON SPECTROSCOPY. In: Vij D. (eds) Handbook of Applied Solid State Spectroscopy. *Springer*, Boston, MA. https://doi.org/10.1007/0-387-37590-2_11

[58] D. T. Larson, L. A. Lott, and D. L. Cash, "Surface Film Thickness Determination By Reflectance Measurements." *Applied Optics*, vol. 12, no. 6, pp. 1271–1275, 1973. [Online]. Available: http://www.ncbi.nlm.nih.gov/pubmed/20125509

[59] Breiland, W. G. and Killeen, K., P., "A virtual interface method for extracting growth rates and high temperature optical constants from thin semiconductor films using in situ normal incidence reflectance*," Journal of Applied Physics*, vol. 78, no. 11, pp. 6726–6736, 12 1995. https://doi.org/10.1063/1.360496

[60] Gordon, P., G., Kurek, A. and Barry, S., T., Trends in Copper Precursor Development for CVD and ALD Applications, 2015 *ECS J. Solid State Sci. Technol.* **4** N3188. https://doi.org/10.1149/2.0261501jss

[61] Cavallotti, C., Gupta, V., Sieber, C., and Jensen, K., F., "Dissociation reactions of CuI(hfac)L compounds relevant to the chemical vapor deposition of copper," *Phys. Chem. Chem. Phys.*, vol. 5, no. 13, pp. 2818–2827, Jun. 2003. https://doi.org/10.1039/B300895A

[62] Thompson, S.C., Cole-hamilton, D.J., Gilliland, D.D., Hitchman, M.L. and Barnes, J.C. (1992), Stable and volatile β-diketonate complexes of copper, calcium, strontium, barium and yttrium for use as chemical vapour deposition precursors. *Adv. Mater. Opt. Electron*., 1: 81-97. https://doi.org/10.1002/amo.860010206

[63] S.-W. Kang, J.-Y. Yun, and Y. H. Chang, "Growth of Cu Metal Films at Room Temperature Using Catalyzed Reactions", *Chem. Mater*. 2010, 22, 1607–1609 1607. https://doi.org/10.1021/cm902294e

[64] C. Guillén, J. Herrero. Single-phase Cu2O and CuO thin films obtained by low-temperature oxidation processes *J. Alloys Compd.* (2018). https://doi.org/10.1016/j.jallcom.2017.12.174

[65] Zanatta, A. & Chambouleyron, I. Absorption edge, band tails, and disorder of amorphous semiconductors. *Phys. Rev. B* 53, 3833–3836 (1996). https://doi.org/10.1103/PhysRevB.53.3833

[66] Anderson, P. W. Absence of diffusion in certain random lattices*. Phys. Rev*. 109, 1492–1505 (1958) https://doi.org/10.1103/PhysRev.109.1492

[67] Kirsch, P., D., and Ekerdt, J., G., "Chemical and thermal reduction of thin films of copper (II) oxide and copper (I) oxide", *Journal of Applied Physics* 90, 4256-4264 (2001). https://doi.org/10.1063/1.1403675

[68] Cesar, Arturo Masse de la Huerta. Development of the Spatial Atomic Layer Deposition (SALD) technique for the fabrication of p-type thin films of highly conductive copper (I) oxide. Materials Science [cond-mat.mtrl-sci]. Université Grenoble Alpes, 2019. English.

[69] Piegari, A., and E. Masetti. "Thin Film Thickness Measurement: A Comparison of Various Techniques." *Thin Solid Films*, vol. 124, no. 3–4, Feb. 1985, pp. 249–257, https://doi.org/10.1016/0040-6090(85)90273-1

[70] Tammenmaa M et al (1985) Zinc chalcogenide thin films grown by the atomic layer epitaxy technique using zinc acetate as source material. *Thin Solid Films* 124(2):125–128. https://doi.org/10.1016/0040-6090(85)90254-8

[71] Malm J et al (2011) Low-temperature atomic layer deposition of ZnO thin films: control of crystallinity and orientation. *Thin Solid Films* 519(16):5319–5322. https://doi.org/10.1016/j.tsf.2011.02.024

[72] Pung S et al (2008) Preferential growth of ZnO thin films by the atomic layer deposition technique. *Nanotechnology* 19(43):435609. https://doi.org/10.1088/0957-4484/19/43/435609

[73] Yousfi EB, Fouache J, Lincot D (2000) Study of atomic layer epitaxy of zinc oxide by in situ quartz crystal microgravimetry. *Appl Surf Sci* 153(4):223–234. https://doi.org/10.1016/S0169-4332(99)00330-X

[74] Kumar, R., Umar, A., Kumar, G., & Nalwa, H. S. (2017). Antimicrobial properties of ZnO nanomaterials: A review. *Ceramics International*, 43(5), 3940–3961. https://doi.org/10.1016/j.ceramint.2016.12.062

[75] Alebeid, O., K. & Zhao, T., (2017) Review on: developing UV protection for cotton fabric, The *Journal of The Textile Institute*, 108:12, 2027-2039, DOI: 10.1080/00405000.2017.1311201

[76] Qian, Y., Willeke, K., Grinshpun, S., A., Donnelly, J. & Coffey, C., C., (1998) Performance of N95 Respirators: Filtration Efficiency for Airborne Microbial and Inert Particles, *American Industrial Hygiene Association Journal*, 59:2, 128-132, https://doi.org/10.1080/15428119891010389

[77] Konda, A.; Prakash, A.; Moss, G. A.; Schmoldt, M.; Grant, G. D.; Guha, S. Aerosol Filtration Efficiency of Common Fabrics used in Respiratory Cloth Masks. *ACS Nano* 2020, 14, 6339−6347. https://doi.org/10.1021/acsnano.0c03252

[78] Yim, W., Cheng, D., Patel, S., H., Kou, R., Meng, Y., S., and Jokerst, J., V., KN95 and N95 Respirators Retain Filtration Efficiency despite a Loss of Dipole Charge during Decontamination, *ACS Applied Materials & Interfaces* 2020 *12* (49), 54473-54480 https://doi.org/10.1021/acsami.0c17333

[79] https://www.cdc.gov/niosh/docs/96-101/default.html

[80] Lee BU. Minimum Sizes of Respiratory Particles Carrying SARS-CoV-2 and the Possibility of Aerosol Generation. *Int. J. Environ. Res. Public Health*. 2020; 17(19):6960. https://doi.org/10.3390/ijerph17196960

[81] Schreer, A., Tinson, C., Sherry, J., P., Schirmer, K., Application of Alamar blue/5-carboxyfluorescein diacetate acetoxymethyl ester as a noninvasive cell viability assay in primary hepatocytes from rainbow trout *Anal. Biochem*., 344 (1) (2005), pp. 76-85. https://doi.org/10.1016/j.ab.2005.06.009